NBSIR 87-3601

High Temperature Chemistry of Stored Chemical Energy Reactions for Propulsion

L. P. Cook, E. R. Plante, D. W. Bonnell, and J. W. Hastie

U.S. DEPARTMENT OF COMMERCE
National Bureau of Standards
Institute for Materials Science and Engineering
High Temperature Chemistry
Ceramics Division
Gaithersburg, MD 20899

July 1987

Annual Report

U.S. DEPARTMENT OF COMMERCE
NATIONAL BUREAU OF STANDARDS

NBSIR 87-3601

HIGH TEMPERATURE CHEMISTRY OF STORED CHEMICAL ENERGY REACTIONS FOR PROPULSION

L. P. Cook, E. R. Plante, D. W. Bonnell, and J. W. Hastie

U.S. DEPARTMENT OF COMMERCE
National Bureau of Standards
Institute for Materials Science and Engineering
High Temperature Chemistry
Ceramics Division
Gaithersburg, MD 20899

June 1987

Annual Report

U.S. DEPARTMENT OF COMMERCE, Malcolm Baldrige, *Secretary*
NATIONAL BUREAU OF STANDARDS, Ernest Ambler, *Director*

High Temperature Chemistry of Stored Chemical Energy Reactions for Propulsion

Annual Report

For the Period May 25, 1985 to December 31, 1986

L. P. Cook, E. R. Plante, D. W. Bonnell, and J. W. Hastie

Ceramics Division
Institute for Materials Science and Engineering
National Bureau of Standards
Gaithersburg, MD 20899

March 25, 1986

Prepared for the Department of the Navy
Office of Naval Research
Arlington, VA 22217

Under Contract No: N00014-85-F-0144

HIGH TEMPERATURE CHEMISTRY OF STORED CHEMICAL ENERGY
REACTIONS FOR PROPULSION
Table of Contents

Abstract 3

I. INTRODUCTION 4

II. REACTION VERIFICATION 6
A. Equilibrium Among Predicted Product Phases 6
B. LiAlMg/ClO_3F 7
C. Thermal Decomposition of ClO_3F 9
i. Coupling of the Thermoanalyzer with a Mass Spectrometer . . 9
ii. Analysis of ClO_3F Decomposition Using High Pressure Sampling Transpiration Mass Spectrometry 11

III. KINETICS 14
A. Reaction of Al_2O_3 with ClO_3F 14
B. Reaction of MgO with ClO_3F 17
C. Reaction of Mg with ClO_3F 18
D. Reaction of Al with ClO_3F 18
E. Transpiration Mass Spectrometry (TMS) of the Al/ClO_3F Reaction. 21

IV. PHASE EQUILIBRIA 23
A. Condensed Phase Equilibria of the System Li_2O-Al_2O_3 23
i. Melting and Solid Solution Relations 23
ii. Solid State Transition in $LiAl_5O_8$ Spinel 25
B. Condensed Phase Equilibria in the System Li_2O-Al_2O_3-AlF_3-LiF . 26
C. Thermodynamics of Competing Oxidation Reactions 27
D. Reactant/Product Vapor Pressures 31

V. DISCUSSION AND FUTURE DIRECTIONS 32

VI. REFERENCES 33

VIII. FIGURES 51

IX. DISTRIBUTION. 53

HIGH TEMPERATURE CHEMISTRY OF STORED CHEMICAL ENERGY REACTIONS FOR PROPULSION

Abstract

This report summarizes the results of a continuing study of the high temperature chemistry of stored chemical energy reaction systems. The eight fuel/oxidant reactions of interest (including several which are multistage) are: $Li/H_2O, H_2/O_2$; Li/H_2O, NaO_2/H_2O, H_2/O_2; $MgAl/H_2O$, H_2/O_2; $LiAl/ClO_3F$; $LiAlMg/ClO_3F$; $LiBe/ClO_3F$; $Li/C_{11}F_{20}$; LiB/NF_3. Thermodynamic prediction of the products of three of these reactions has been corroborated by equilibrating postulated products at high temperature, while results from a fourth reaction require modification of the reaction scheme originally proposed. Mass spectrometric observations on the thermal decomposition of ClO_3F at elevated temperatures are presented.

Thermogravimetric studies have been completed on the behavior of Al_2O_3 and MgO in the presence of ClO_3F. Based on these data a new ceramic containment system comprised of alumina and magnesia parts has allowed extension of kinetic experiments from the 650°C limit previously encountered to a temperature in excess of 800°C. Using the new apparatus, we have observed the relative inertness of the Al component of the fuel to oxidation by ClO_3F even at 800°C. We have also noted the extensive vapor phase transport of LiF and MgF_2, not expected on the basis of known thermodynamic data.

Thermogravimetric experiments have been completed on the oxidation of molten aluminum droplets by ClO_3F. Rate data for this reaction indicate multiple mechanisms, possibly including the following steps: (1) nucleation and growth of AlF_3 precipitation sites; (2) edge growth of AlF_3 islands followed by coalescence of islands; (3) diffusion limited thickening of the AlF_3 layer. Observations on the early stages of the Al/ClO_3F reaction have also been made using high pressure sampling transpiration mass spectrometry.

Phase equilibrium experiments have continued on the product system Li_2O-Al_2O_3 in sealed Mo capsules, utilizing an improved high temperature equilibration apparatus. Experiments indicate a previously undescribed degree of complexity near the high alumina end, which may involve solid solution of Li_2O in the corundum structure, or an intermediate series of solid solutions or compounds based on the $LiAl_5O_8$ spinel phase. The solid state phase transition in $LiAl_5O_8$ has been studied by DTA; although the solid solution region is small, the temperature of this transition ranges from 1269° to 1308° depending on whether it is Al_2O_3-saturated or Li_2O-saturated. In the ClO_3F-based reaction systems, substantial entry of fluorine into the product $LiAl_5O_8$ spinel phase is postulated.

Thermodynamic calculations have been completed to assess the importance of vaporization over reactant/product solids and liquids. In a situation where dissociated ClO_3F is flowing over molten alloys, fluoride products are thermodynamically most stable, followed by oxides, and finally by chlorides. The chlorides in general have high vapor pressures, which may be enhanced by

polymerization. If passivating product layers of liquid or solid fluorides are formed on metal reactants during ClO_3F oxidation, it would be expected that chlorine and chlorides would be partitioned strongly into the vapor phase, along with oxygen.

Future work is planned which will determine rate constants and temperature dependencies for the kinetics of the oxidation of individual alloy components by Cl_2, O_2 and F_2. Phase equilibrium determinations will focus on the system Li-Al-Mg-O-F, with special regard to the entry of fluorine into oxide phases.

I. INTRODUCTION

The present report describes results of our research on the chemistry of liquid metal-based stored chemical energy propellants during the past year. This work represents a continuation of work begun earlier and described in two previous reports [1, 2], where extensive literature searches were also reported. There are at least eight different stored chemical energy propulsion (SCEPS) reactions involving various fuel/oxidant pairs which are of interest. Several of these reactions involve more than one stage. Reactions or reaction groups considered are:

$$\left.\begin{aligned} 2\ Li(\ell) + H_2O(g) &\rightarrow 2\ LiOH(\ell) + H_2(g) \\ H_2(g) + (1/2)\ O_2(g) &\rightarrow H_2O(g) \end{aligned}\right\} \qquad (1)$$

$$\left.\begin{aligned} 2\ Li(\ell) + H_2O(g) &\rightarrow 2\ LiOH(\ell) + H_2(g) \\ (2/3)\ NaO_2(c) + (1/3)\ H_2O(g) &\rightarrow (2/3)\ NaOH(c) + (1/2)\ O_2(g) \\ H_2(g) + (1/2)\ O_2(g) &\rightarrow H_2O(g) \end{aligned}\right\} \qquad (2)$$

$$\left.\begin{aligned} 2\ MgAl(\ell) + 5\ H_2O(g) &\rightarrow MgO(c) + MgAl_2O_4(c) + 5\ H_2(g) \\ 5\ H_2(g) + (5/2)\ O_2(g) &\rightarrow 5\ H_2O(g) \end{aligned}\right\} \qquad (3)$$

$$2\ LiAl(\ell) + ClO_3F(g) \rightarrow Al_2O_3(c) + LiF(c) + LiCl(\ell) \qquad (4)$$

$$4\ LiAlMg(\ell) + 3\ ClO_3F(g) \rightarrow MgF_2(c) + LiF(c) + 3\ LiCl(\ell) + 2\ MgAl_2O_4(c) + MgO(c) \quad (5)$$

$$8\ Li(\ell) + 8\ Be(c) + ClO_3F(g) \rightarrow 8\ BeO(c) + Li_2O(c) + 3\ LiF(c) + LiCl(\ell) \quad (6)$$

$$C_{11}F_{20}(g) + 20\ Li(\ell) \rightarrow 11\ C(c) + 20\ LiF(c) \quad (7)$$

$$2\ Li(\ell) + LiB(c) + NF_3(g) \rightarrow 3\ LiF(c) + BN(c)\ . \quad (8)$$

Preliminary kinetic data on many of these reactions have been presented in an earlier report [2]; however results were limited to 650°C by reaction of the experimental container materials with oxidant (usually ClO_3F) and/or with liquid metal. In this report experiments up to 800°C are described.

Reference [1] has dealt with phase equilibria in the system Li_2O-Al_2O_3. Phases on this join are products in several reaction schemes. In the present report, additional data are presented for the high alumina end of the system. We also discuss equilibration experiments on the thermodynamically predicted reaction products in several of the reactions (1) through (8). These experiments have led to the postulation of extensive fluorine substitution in at least one oxide phase. Finally, experimental results indicate the widespread importance of the gas phase as a transport medium, and we report mass spectrometric measurements on the gas phase, including the use of a high pressure mass spectrometry system developed in this laboratory. Supplementing these measurements are thermodynamic calculations of vapor pressures over products and

reactants at high temperatures for the various reaction schemes. Plans for follow-up research are given in the concluding section.

II. REACTION VERIFICATION

A. Equilibrium Among Predicted Product Phases

Thermodynamically predicted products of various reactions from ref. [2] are given in Table 1. Results of experiments on reactions (1), (2), and (3) were given in ref. [2]; reaction (6) will not be investigated experimentally due to the toxicity of beryllium. Because of the kinetic and materials limitations indicated in this and previous reports, it has not yet been possible to obtain direct data on reactions (4), (5), (7), and (8) to test the thermodynamic predictions. An indirect, though inconclusive test involves heating mixtures of the predicted products; if they do not react, this is consistent with the equilibrium predictions; however this circumstance is not proof, as kinetic factors could impede the attainment of equilibrium. Predicted products of reactions (4), (7), and (8) have been mixed together in equal parts by weight and equilibrated. Experimental results are shown in Table 2. These experiments were completed in a box furnace in sealed Pt capsules. Specimens were removed from the furnace and cooled in air (unless otherwise noted), then opened and x-rayed. Results for reactions (4) indicate formation of a spinel phase resembling $LiAl_5O_8$, at 1000°C and 1200°C; reaction (4) is therefore not correct as written. As the alumina has vanished, and no other new phases are present, entry of fluorine into the spinel phase is a possibility, perhaps as a solid solution of the form $Li_{(1+x)}AlAl_{(4-x)}O_{(8-2x)}F_{2x}$. This possibility will

be discussed further in Section IV-B. The implication of the formation of oxyfluoride phases on the predicted energy yield of reaction (4) cannot be assessed without additional thermodynamic data. Reactions (7) and (8), however, may be correct as written, as the predicted products: LiF + C, and LiF + BN, respectively, show no sign of reaction when heated.

B. LiAlMg/ClO_3F [reaction (5)]

In reference [2] we described experiments on the LiAl/ClO_3F reaction pair, which were limited by the inability to exceed temperatures above 650°C, due to reaction of the molten fuel with the alumina; since that time we have investigated the use of MgO as a container, and it appears to function much better. The initial experiments done with this system utilized an MgO cup, into which was placed a small (25 mg) coupon of LiAlMg ternary alloy. The coupon was sliced from an ingot of alloy prepared by induction melting of the elemental constituents under an argon atmosphere in a tantalum crucible, followed by casting in a copper chill mold. The sample was placed in a Mettler[1] TA-1 thermal analysis system on a magnesia substrate. First the sample was brought to a temperature of 800°C under argon. As the temperature was increased, relatively little weight change was noted, indicating that the activity of the Mg component in the alloy was sufficiently lowered to prevent the rapid volatization that would be experienced for pure Mg at this

[1]Certain commercial equipment, instruments, or materials are identified in this paper in order to adequately specify the experimental procedure. Such identification does not imply recommendation or endorsement by the National Bureau of Standards.

temperature (refer to Fig. 36). After temperature was reached, ClO_3F gas was introduced at a constant flow rate of 2.5 cc/min. A rapid and relatively constant rate of weight gain was observed, which abruptly halted after approximately 1/2 hour. Upon examination of the charge, an intergrown felt-like mass of acicular crystals rimming the cell was observed. All that remained of the alloy coupon was a small metallic button. X-ray diffraction analysis of the felted mass of crystals indicated primarily MgF_2 with lesser LiF. No x-ray evidence of aluminum-containing phases was found in the crystalline mass. The metallic button is assumed to have been highly enriched in aluminum (an analysis was not possible). During this experiment a platinum gas feeder tube was used, as this had worked well at 650°C. However at the 800°C temperature of this experiment, platinum transport was observed and so subsequent experiments used an alumina feeder tube for the ClO_3F (Section III-A).

The apparent transport of lithium and magnesium away from the reaction site in the presence of ClO_3F or its dissociation products is not predicted on thermodynamic grounds as the vapor pressures of the thermodynamically most stable salts such as LiF and AlF_3 are relatively low at 800°C (see section IV-D). A possible explanation is that kinetic factors impede the development of a surface layer of the predicted equilibrium fluorides of Mg and Li. Several possible reactions for transport of Li and Mg based on known vapor species exist. Some of these possibilities are indicated in Table 3 (alternative explanations, to be examined in future work, involve possible formation of new vapor complexes). Metal vaporization does not appear to be the principal

mechanism, as there was not substantial weight loss from the ingot prior to the time the ClO_3F flow was initiated. Metastable formation of chloride species (including dimers, though these are not shown), is a mechanism that could lead to enhanced transport from the reaction site, as the chlorides of lithium and magnesium both have substantially higher vapor pressures than the fluorides (section IV-D). The fact that aluminum apparently did not migrate in this experiment may indicate the relative ease of formation of AlF_3. Experiments described in a later section (III-C) point up the effectiveness of a very thin layer of crystalline AlF_3 in preventing further reaction. Furthermore, AlF_3 is solid at the temperature of the experiment, whereas the fluorides of Mg and Li are molten, and would presumably facilitate diffusion of metal species to the reaction site.

C. Thermal Decomposition of ClO_3F

i. Coupling of the Thermoanalyzer with a Mass Spectrometer

Failure of the Pt transport tube initially used to pipe ClO_3F into the hot reaction zone on the thermal analysis system occurred soon after the first experiments were conducted at 800°C. Extensive thinning of the tube due to Pt removal from the inside and apparent redeposition near the exit point of the ClO_3F gas was observed. Formation of a platinum halide species was therefore suggested, which in turn implies decomposition of the ClO_3F gas. The platinum feeder tube was replaced by alumina, which has performed much better. Observations suggest that a thin relatively stable layer of microcrystalline solid AlF_3 is formed on the surface of the alumina, which prevents further reaction of the alumina. Crucibles

of alumina for the experiments with ClO_3F could thus be "presaturated" to constant weight together with their MgO inserts (if used) at the temperature of the experiment in flowing ClO_3F (this is discussed more fully in Sections III-A, B). Alloy starting materials were then added and the alloy reaction with ClO_3F studied as outlined above in Section II-A. Formation of fluoride reaction products in these experiments with apparent lack of any oxide phases suggested that only selected species within the gas phase were reacting, again raising the possibility of thermal decomposition of the ClO_3F. According to the literature (refs. [3, 4]) ClO_3F does not decompose up to the softening point of glass (e.g. 820°C for type 7740 Pyrex), even though it is thermodynamically unstable above 25°C, according to data from JANAF [5].

In order to gather evidence for gaseous decomposition products, a leak valve was installed in the exhaust line of the thermal analysis system and a small portion of the exhaust gas was bled into the source of a modulated beam mass spectrometer system. Separate experiments with ClO_3F at room temperature indicate that electron bombardment at 30 eV forms the parent and fragment ions, in order of decreasing intensity, ClO_3^+, ClO_2^+, ClO^+, ClO_3F^+, and Cl^+. These ions, with the exception of the parent ClO_3F^+, are a typical fragmentation pattern expected from electron impact with ClO_3F parent molecules.

Fig. 1 shows ion intensities as a function of temperature scaled using the $^{40}Ar^+$ intensity as a reference (normalized to 100). These observations were made after the prefluorination reaction had taken place

as indicated by the constancy in mass of the alumina cell. There is a large change in O_2^+ intensity between 500 and 700°C. Also to be noted are the signals due to Cl_2^+ and ClF^+ at 700°C. Near 500° the Cl_2^+ and ClF^+ signals are very weak, and signals due to the normal fragmentation pattern of ClO_3F dominate the spectrum. Our interpretation of these data is that thermal decomposition of ClO_3F takes place between 500 and 700°C. The formation of Cl_2^+ and ClF^+ probably is due to recombination of Cl and F formed in the decomposition reaction, as they are not normally formed by fragmentation of ClO_3F. Also, the unusual behavior of the higher temperature part of the ClO^+ curve would be consistent with it being formed from recombination of decomposition products.

ii. Analysis of ClO_3F Decomposition Using High Pressure Sampling Transpiration Mass Spectrometry

We have developed in our laboratories a high pressure sampling mass spectrometric instrument for studying gas/solid interactions[6]. This instrument couples the classical transpiration method with a molecular beam mass spectrometric analysis of the reaction vapor species. In this technique, also known as transpiration mass spectrometry (TMS), gases formed in the reaction zone are expanded through a nozzle into a high vacuum system, where gases in the beam are mass analyzed [Fig. 2]. The expansion through the nozzle leads to the formation of a beam with a frozen vapor species composition representing the equilibrium or steady-state concentrations present the reaction cell.

A significant advantage of use of the TMS system over the classical Knudsen effusion method is that it allows measurements to be made at pressures, approaching one atmosphere. This pressure region is much closer to that present in operating propulsion systems. Because of beam dynamics and the relatively high background pressures in the mass spectrometer section of the system, reactor pressures generally need to be in the range 10^{-4} atm and above before they can be observed. The system is usually operated as a fixed flow system and the flow rate as well as the total pressure are monitored during the experiment. The measured total pressure and mass spectral ion intensity of the carrier gas can be used to calibrate the system sensitivity and to determine the partial pressures of other species formed in the reaction cell, as described in ref. [6].

The thermal decomposition of ClO_3F, as noted in section (i), leads to problems in data interpretation because of the possible recombination processes that may take place between the thermal analysis system and the mass spectrometer detector. The relatively long transit time between decomposition and detection is effectively eliminated by using the sampling system.

The decomposition of ClO_3F was observed in the TMS system by introducing ClO_3F into a fused silica transpiration reactor using argon as the carrier gas. The data obtained from these measurements is shown in Fig. 3 where the lines shown represent what we would expect for an experiment in which the scatter in the data is averaged out. The actual

data have considerable scatter owing to technical problems resulting from decreases required in the flow rates initially selected in order to maintain the pressure in the optimum range. The change in flow rates results in relatively long time lags before the gas composition has had an opportunity to shift to new composition values because of the relatively small flow rate and large volume of the system.

The appearance of Cl_2 and O_2 as indicated by the ions Cl_2^+ and O_2^+, together with the concomitant disappearance of ClO_3F^+ and its fragment ions, indicates the decomposition of ClO_3F in the temperature range of 400-600°C. Comparison of the $^{37}ClO_3^+$ and $^{35}ClO_3^+$ isotopic ion intensities indicates formation of an additional species of the same mass of 85μ (mass units) as $^{37}ClO_3^+$ at temperatures above about 400°C. The most reasonable assignment for this species is $^{28}SiF_3^+$ which arises from SiF_4 produced by reaction of F_2 with the silica reaction cell. This species accounts for the apparent absence of F_2 as a ClO_3F decomposition product, whereas Cl_2 and O_2 are observed. It can be noted that several ions (ClF^+ and ClO^+) observed in the thermoanalyzer mass spectrometer experiment were not observed in the TMS measurements which indicates that these species were probably formed by reaction of decomposition products during the relatively long transit time from the thermoanalyzer to the mass spectrometer system.

Complementary TMS data were obtained in the absence of a carrier gas. As noted above, the total pressures observed at constant flow rate are generally monitored during the measurements. These data also indicate

thermal decomposition of ClO_3F in a similar temperature region to that noted in the Ar carrier gas experiments, as shown in Fig. 4. For a nondecomposing gas, a plot of pressure versus temperature will give a straight line whose slope is related to the number of moles per unit time flowing through the system. Note that in Fig. 4 there is a break in the curve near 530°C, with pressures below and above this temperature being represented reasonably well by straight lines. The ratio of the slopes is 2.8 which is reasonably close to the ratio of the number of moles of gas of the products to reactants for the reaction,

$$4\ ClO_3F(g) + SiO_2\ (\text{fused quartz}) = 2\ Cl_2(g) + 7\ O_2(g) + SiF_4(g).$$

At the same time the pressure-temperature data was obtained the ion current from $^{35}ClO_3^+$ was observed. These data are plotted in Fig. 5. The scatter in the low temperature region of the curve is a presently unexplained phenomenon which is apparently a result of changing the temperature.

III. KINETICS

A. Reaction of Al_2O_3 with ClO_3F

Upon failure of a Pt feeder tube used for the ClO_3F, it was decided to test high purity alumina as a replacement, as this is commercially available in tubing of several sizes. To establish the long term behavior of Al_2O_3 in flowing ClO_3F at high temperature a series of thermogravimetric experiments was carried out. First it was noted that unused alumina crucibles could be heated to nearly constant weight in

flowing ClO_3F (see Fig. 6). Windowless SEM/EDX analysis revealed the presence of a coating of faceted crystals giving a strong fluorine signal. This was interpreted as indicating development of an AlF_3 coating. Presumably once formed this coating served as a diffusion barrier against further reaction. Assuming uniform formation of AlF_3 on the inner surface of the alumina crucible of Fig. 7 an estimate of film thickness formed at 800°C would be about 10 μm.

To further explore the stability of Al_2O_3 in flowing ClO_3F, experiments at temperatures from 450° to 800°C were conducted using 0.3 μm powders of Linde A alumina (99% corundum). Results are shown in Fig. 7 and Table 4. In these experiments, the samples were first brought to temperature and then the gas was introduced. X-ray powder diffraction analysis of the product indicated only AlF_3. From Table 4, it can be seen that as the temperature reaches 700°C the weight gain approaches the theoretical value of 64.7% for complete conversion of the alumina powder according to the reaction:

$$Al_2O_3(c) + 3\ F_2(g) \rightarrow 2\ AlF_3(c) + 3/2\ O_2(g)\ .$$

The effect of varying the rate of ClO_3F flow over the powdered alumina at 800°C is shown in Fig. 9. Although the rate of reaction, and hence the slope of the reaction curves vary, all show a well-defined reaction end point, which occurs at a weight gain of 93-94% of that for complete conversion to AlF_3 (see Table 5). A substantial part of the reaction

curves in Figs. 7-9 can be approximated by a parabolic rate law of the type:

$$\left(\frac{W}{A}\right)^2 = kt$$

where W/A is the mass gained per unit area available for reaction , k is the rate constant and t is the cumulative reaction time. Calculated rate constants for the data in Figs. 8 and 9 are given in Table 6, and the portions of the data which have been fitted in this way are indicated in the illustrations. Note that the early portions cannot be fitted in this fashion; the reason for this is not clear, but it may have to do with nucleation and growth of AlF_3 product. The point at which the powdered alumina is consumed (reaction end point) is obvious on Figs. 8 and 9. In the lower temperature (450-600°C) experiments in Fig. 7, where a reaction end point is not observed, the rate constants show an Arrhenius relationship, as illustrated in Fig. 9. The equation of the line is

$$\log k = 7.63 - 7.06 \times 10^3 / T(K).$$

Above 600° this relationship is not followed, although the higher-flow rate experiments give k's which lie closer to the Arrhenius line. This implies that above 660°C, under the given experimental conditions, the supply of ClO_3F to the reaction interface may be the rate limiting factor for these high surface area experiments. It should be noted that the initial surface area used in plotting Figs. 7 and 8, based on information provided by the manufacturer of Linde A, was 10-18 m^2/g; an average of 14 m^2/g was used. In practice, this value may have been appreciably reduced as the sample heated up and as the reaction proceeded. This is also indicated by an attempt to calculate the thickness of the reaction

layer on the powders, which gives a value a factor of 10 too low to be consistent with the nearly complete reaction of the 0.3 μm powders, as observed above 600°C.

B. Reaction of MgO with ClO_3F

In a later section (IV-C) we describe the results of thermodynamic predictions for the interaction between MgO, Cl_2 and F_2. The net result is that MgF_2 should form at the expense of MgO. Experiments were conducted on the thermoanalyzer to assess the importance of these reactions in the presence of ClO_3F (or its dissociation products) at 800°C.

Results of an experiment using a coarsely crystalline MgO cell are shown in Fig. 10, which indicates a "saturation" effect similar to that described above for Al_2O_3. Presumably this is due to formation of a thin layer of MgF_2 which impedes further reaction, according to:

$$MgO(c) + F_2(g) \rightarrow MgF_2(c) + (1/2)\ O_2(g)$$

Results obtained for crucibles fabricated of dense, polycrystalline sintered magnesia are similar. Experiments in which the flow rate of ClO_3F was varied during saturation of a polycrystalline cell show a nearly linear correlation between flow rate and rate of reaction. For the coarsely crystalline cell the calculated thickness of the MgF_2 layer after 1 hour, is approximately 2 μm. As indicated, the final part of the data in Fig. 10 fit a parabolic rate law.

C. Reaction of Mg with ClO_3F

A thermogravimetric experiment was attempted in which Mg metal was heated to 800°C, preparatory to reaction with ClO_3F. However the vapor pressure of Mg metal at temperatures above its melting point is such that significant evaporation occurs at the metal surface (see section IV-D), and for this reason it was not possible to complete the experiment at 800°C. To minimize metal vaporization and obtain meaningful data, it may be necessary to complete future experiments at temperatures only slightly above the melting point of Mg (650°C).

D. Reaction of Al with ClO_3F

Once it was established that the ClO_3F decomposed at elevated temperatures, that the individual components of the Al-containing alloys react somewhat independently, and that Al does not react to the same degree as the other metal components, it was decided to focus more specifically on the problem of Al reaction by working with the pure metal. For quantitative reproducible kinetic studies, the following requirements are essential: minimization of experimental geometry effects; and constancy or quantification of relevant variables such as surface temperature, surface area, oxidant flow rate and ambient pressure. Surface area was made constant by selecting high purity aluminum-shot pieces of similar weight. It was found that these formed a nearly spherical ball (Fig. 11) in the Al_2O_3 crucible when melted, giving relatively constant surface area. During ClO_3F experiments at 800°C, all Al droplets showed a "frosting" of the surface, which at higher magnification in the SEM proved to be a dense interlocking mass of well-

faceted crystals (Fig. 12). SEM/windowless EDX showed Al and F, suggesting AlF_3.

In the Al reaction experiments the proximity of the ClO_3F flow tube to the reaction surface was important. In the case where the exit port was ~10 mm from the surface of the molten Al droplet, a tear-shaped channel, free of surface salts was formed, regardless of flow rate (Fig. 13). When the exit port was moved to ~15 mm from the surface, then no such salt-free channel was formed, although the surface of the ball had slight creases directly under the exit port. The reason for the salt-free scar at the close-in geometry is not clear. It is tempting to suggest a physical effect associated with the velocity of the inlet gas, however, this would be ordinarily thought to result in increased formation of salt so that any physical disturbance of the surface of the Al would be rapidly covered over by salt crystals (e.g., as seen in Fig. 12). The deep scar shown in Fig. 13, typical of experiments at the close-in geometry, is suggestive of removal of material from the surface of the Al. This would require both local formation of a volatile Al species and local suppression of the salt formation (presumably AlF_3) seen on the rest of the surface. A possible chain of events at the close-in geometry might be (assuming dissociation of the ClO_3F):

$$(3/2)\ Cl_2(g) + Al(\ell) \rightarrow AlCl_3(g) \qquad (13)$$

$$AlCl_3(g) + (3/2)\ F_2(g) \rightarrow AlF_3(c) + (3/2)\ Cl_2(g) \qquad (14)$$

with the solid being precipitated away from the high flow area on the droplet surface. Hopefully this possibility can be tested using transpiration mass spectrometry.

Thermogravimetric rate data for reaction of liquid Al with ClO_3F at 700, 750 and 800°C are shown in Fig. 14 and summarized in Table 7. The flow rate was nominally 1 sccm. The shapes of the three curves in Fig. 15 are similar, but the amplitude (total wt. gain of the Al droplets) increases by a factor of about seven going from 700 to 850°C. The highest total weight gain (800°C experiment) is nonetheless small (2.75 mg) by comparison with a typical droplet weight (415 mg).

The effect of flow rate on reaction of ClO_3F with Al at 800°C is shown in Fig. 15 and summarized in Table 8. At the highest flow rate the shoulder in the curve is considerably rounded and the slope leading up to it is steeper relative to the two lower flow rates.

The curves in Figs. 14 and 15 are somewhat more complex than the Al_2O_3/ClO_3F curves of Figs. 7 and 8. Preliminary interpretation can be made in terms of three different processes, each dominant in a different area of the curve: (a) initial region: nucleation and growth of AlF_3 reaction sites; (b) middle region (nearly linear, to parabolic as shoulder is approached) lateral growth of AlF_3 islands at their edges, followed by merging of islands and complete coverage of the surface; (c) final region (parabolic): thickening of dense AlF_3 film by diffusion through the film. A summary of the mathematical analysis of the data is given in Table 9.

E. Transpiration Mass Spectrometry (TMS) of the Al/ClO_3F Reaction

In measurements described in ref. [2], in which we examined the behavior of pure Al metal with ClO_3F using a gas entry Knudsen effusion method, the masses identified were AlF^+, $AlCl^+$, AlF_2^+, $AlClF^+$, AlF_3^+, AlF_2Cl^+, $AlCl_2F^+$, and $AlCl_3^+$. The period during which aluminum halide species were generated was quite short and the fraction of the sample which reacted was small. It was presumed that the sample became less reactive with time because of formation of either an Al_2O_3 or an AlF_3 surface layer.

More recently, we have carried out TMS measurements on the Al/ClO_3F reaction. These experiments were carried out in the absence of a carrier gas. A fragment of pure Al shot was placed in a MgO boat inside the fused silica transpiration cell. ClO_3F was introduced, and the product gases were analyzed mass spectrometrically. Ion intensities at 729°C are indicated in Table 10. Aluminum bearing vapor species were observed from 667 to 736°C. All of the ions identified in the Knudsen experiment with the exception of AlF_3^+ were detected; the vapor concentration of $AlF_3(g)$ in the above temperature range would be below the detection limits of the mass spectrometer. Also O_2^+, Cl_2^+ and SiF_3^+ were observed during this period. The experiment was terminated because a significant decrease had taken place in all the ion signals as well as the total pressure. This behavior is not presently understood because the total pressure should have remained at least as high as that due to decomposition of ClO_3F unless erosion of the expansion nozzle took place or the unblocking of a partially blocked nozzle took place.

It seems clear from the results of this experiment that the reaction of Al with ClO_3F takes place to a greater extent than was observed in the Knudsen effusion case at lower pressures. The remaining sample was removed from the magnesia cell at the conclusion of the experiment and observed to be covered with a white layer. An SEM examination of the surface deposit showed it to consist of columnar crystals aligned at right angles to the reaction surface. A windowless EDX spectrum showed the presence of oxygen, but no fluorine (fluorine was observed in the very top surface layer, however). Aluminum was the dominant constituent, with minor amounts of Mg (from the boat) and Si (from the silica cell). Apparently Al_2O_3 is the principal reaction product which implies that the fluorine activity has locally been reduced near the surface of the Al, thus suppressing the formation of the more stable AlF_3. A likely explanation is reaction of the fluorine component of the oxidant with the silica of the outer reaction cell; this is consistent with observation of silicon fluoride species in the mass spectrum of the exiting gases. Future experiments will utilize a different material for the outer cell. It is hoped that such experiments will also allow closer observation of any kinetic factors influencing the formation of aluminum chloride or fluoride species.

IV. PHASE EQUILIBRIA

A. Condensed Phase Equilibria of the System Li_2O-Al_2O_3

i. Melting and Solid Solution Relations

Experiments, primarily on the Li_2O-rich end of the system Li_2O-Al_2O_3, were described in Ref. [1]. Many problems remain unresolved on the high

alumina end of the system. Alumina-rich compositions are important for several reasons; they encompass reaction product phases, including $LiAlO_2$ and $LiAl_5O_8$; the thermochemistry of these phases has implications for calculations of energy yield; as products of high stability, they have potential materials applications. The major challenge in working with these materials is the high temperature of the relevant equilibria, coupled with the non-quenchability of the samples. We have developed and refined a high temperature apparatus and methodology for dealing with these problems, as follows.

After homogenization, powdered mixtures were loaded into Mo capsules in a drybox, followed by sealing with a carbon arc welder. Samples (up to eight at a time) were then suspended in a Mo bucket in the hot zone of a tungsten furnace. Temperature was measured with a reinforced W3%Re/W25%Re thermocouple calibrated against the melting points of Pd and Pt and inserted into the Mo bucket in the center of the ring of samples. Generally calibrations were within 5 to 10°C of the correct melting points. Thermal gradients along the length and diameter of the holder were less than 5°C and so total uncertainty in the temperature is near ±15°C to ±20°C, including control variation of ±5°C. Temperature was controlled via a second thermocouple in the base of the furnace. Experiments were terminated by allowing the furnace to cool (a typical cooling curve is shown in Fig. 16). Although cooling at this rate is not "quench", it is rapid enough to preserve many of the high temperature textural relationships. Following the experiments, the capsules were opened and products were examined by scanning electron microscopy.

Generally it was possible to differentiate solids which were in equilibrium at the temperature of the experiment by their size (5 to 10 μm) and their well-developed facets. Crystals in equilibrium with melt tended to be somewhat larger than those formed in the absence of melt. Melts, if present, generally occupied the interstices between such crystals, and their microcrystalline descendants could be readily identified as in Fig. 17. Given the fact that the rate of cooling was not "quench", the crystallization history of such melts must be considered in making interpretations. For example the melt phase in Fig. 17 probably crystallized eutectically. Situtations where rims of material have crystallized in an oriented fashion around the larger grains may possibly indicate a peritectic, whereas in equigranular, porous specimens with sharp grain boundaries, melt was apparently never present. Using data of this sort the diagram in Fig. 18 was developed. The apparent lack of melting at temperatures below 1950°C for Al_2O_3-rich compositions could mean either presence of a compound intermediate between $LiAl_5O_8$ (most probably with incongruent melting), solid solution based on alumina, or possibly both. There is no x-ray evidence for solid solution or intermediate compounds; hence it is postulated that if such phases do exist they are unstable at lower temperatures, and decompose to a mixture of lithium spinel and corundum. Microstructural evidence for such decomposition is seen in the lamellar structure of Fig. 19.

ii. Solid State Transition in $LiAl_5O_8$ Spinel

At lower temperatures the $LiAl_5O_8$ spinel phase undergoes a phase transition apparently related to ordering of Li and Al on the octahedral

spinel sites. A Rietveld refinement of the structure of $LiAl_5O_8$ based on neutron diffraction data was given in reference [1]. This indicated essentially complete ordering of Li and Al in the octahedral sites, with no tetrahedral Li. Although this specimen had been equilibrated at about 1600°C, apparently it was not cooled rapidly enough to freeze in the disordered state. Hence we still do not have good structural data on the high temperature disordered stage. During the past year, experiments were conducted on compositions from 50 to 100 mole% Al_2O_3, to study in more detail the postulated order/disorder transition in $LiAl_5O_8$. The phase transition was observed to be reversible (Fig. 20). Upon cooling, the transition was relatively sluggish and required supercooling of about 25°C for initiation of the reaction at 1280°C which then apparently continues down to 1090°C. Upon heating, a well-defined single thermal event was seen. The values of the heating event were used to define the temperature of the transition, as described in Ref. (1). Nine compositions were studied; temperatures of the transition were constant, but different on either side of the spinel composition (see Fig. 21). This implies that a slight degree of solid solution in the 1:5 composition exists, which nevertheless has a very pronounced effect (nearly 30°C) on the transition. The effect of annealing at temperatures above and below the phase transition on the x-ray powder pattern is manifested in the intensity ratios of several of the lines, which is consistent with an order/disorder transition.

B. Condensed Phase Equilibria in the System Li_2O-Al_2O_3-AlF_3-LiF

As noted above in Section II-B, experiments to verify the products of reaction (4) suggested the existence of a spinel phase containing fluorine. Several experiments have been conducted to follow up this possibility, which is of both crystal-chemical interest and also of importance to the rheological properties of predicted solid/liquid products. Assuming that there are no anion vacancies, fluorine substitution can be plotted in the ternary reciprocal system Li,Al//F,O.

Experiments on the compositions plotted in Fig. 22 have been completed at 1200°C in the system. The purpose of these experiments has been to locate a single-phase region of fluorine-substituted spinel. Evidence for lack of the expected degree of melting at 1200°C in most compositions on the Li_2O-rich side of the LiF-Al_2O_3 join in the ternary reciprocal system Li_2O-Al_2O_3-AlF_3-LiF comes from: visual observation, SEM high magnification examination, and powder x-ray diffraction data. Since the minimum melting temperature along the join LiF-AlF_3 is 710°C, it would be expected that fluoride phases would be present as melts at the experimental temperature. The x-ray data are somewhat ambiguous; nearly all experimental results give weak lines at positions corresponding to the major lines for LiF and Li_3AlF_6. Possible explanations include: (1) small amounts of unreacted salt; (2) small amounts of equilibrium melt; (3) superstructure lines which happen to fall at the LiF and Li_3AlF_6 positions. Possibility (2) is judged most likely. On the basis of intensities of LiF and Li_3AlF_6 lines, compositions near

75($2LiF.Al_2O_3$): 25($LiAl_5O_8$) are nearly single phase. Results of SEM examination of a series of 1200°C quench experiments along the join $LiAl_5O_8$-($LiF.Al_2O_3$) indicate that with increasing LiF concentration, the fraction of well-faceted spinel crystals increases until at 75 ($2LiF.Al_2O_3$): 25($LiAl_5O_8$) the sample is comprised almost entirely of well-faceted spinel crystals (Fig. 23-a). On the other hand, at the $2LiF.Al_2O_3$ composition, evidence for a melt is clear at high magnification (Fig. 23-b). The interpretation of the SEM and x-ray observations is summarized in the 1200°C isothermal phase diagram of Fig. 24.

C. Thermodynamics of Competing Oxidation Reactions

Some experimental observations made during this work indicated that selective reactions were taking place. For example, ClO_3F reaction with a Li/Al alloy tended to form only halides with no indication of oxide formation. Also, during reaction for ClO_3F with a Mg alloy, MgF_2(c) was observed to have been transported to the side of the reaction crucible even though the vapor pressure of MgF_2 was too low to account for the transport at 800°C. A possible explanation is that transport was due to $MgCl_2$ which condensed and underwent a halide exchange reaction with F_2. This is evidence that, at least under laboratory conditions, the paths of the chemical reactions are being governed by both thermodynamic and kinetic factors.

To investigate these processes we considered the known thermodynamic data governing these reactions. For purposes of this discussion we will

categorize reactions based on the standard Gibb's energies of formation of the halides and oxides into the following types:

(a) interaction of chlorides and fluorides with metals;

(b) interaction of oxides with fluorine or chlorine;

(c) reaction of chlorides with fluorine;

(d) interaction of chlorides with fluorides;

(e) interaction of oxides with fluorides;

(f) interaction of oxides with chlorides.

Data for these types of reactions are listed in Tables 11 through 16. The tables list the Gibb's energy of the reactions, as written, in calories for temperatures from 800 through 1300 K respectively. As usual, positive free energies indicate that the reactants are the predominant materials present at equilibrium and negative free energies indicate that the products are the predominant materials present. The state selected for the individual substances was based on vapor pressure, melting point and phase equilibrium considerations. Thus, it was assumed that $AlCl_3$ and $BeCl_2$ would be present as gases, that most of the halide reaction products would be liquids, and that oxides except for Li_2O would be present as solids. Effects due to the possible formation of mixed halide species such as $AlClF_2$ have been ignored in the present calculations.

Data in Table 11 correspond to the displacement of a metal from a less stable metal halide to form a more stable metal halide. From the reactions considered it is clear that if equilibrium was maintained

during the reaction the metals would be consumed in the order:

Li>Mg>Be>Al.

Results in Table 12 show that none of the metal oxides are thermodynamically stable in the presence of $F_2(g)$ while only the relatively reactive $Li_2O(\ell)$ is unstable in the presence of $Cl_2(g)$.

Table 13 shows that none of the chlorides are stable in the presence of fluorine and will be converted to fluorides, while Table 14 expresses possible interaction reactions among chlorides and fluorides.

Tables 15 and 16 list possible equilibria for oxide-fluoride and oxide-chloride reactions. These data show which oxide-halide couples are stable or unstable. For example, Al_2O_3 will not react with BeF_2, LiF, or MgF_2; BeO is resistant to LiF; and MgF_2 and MgO are resistant to LiF. On the other hand, MgO is not resistant to AlF_3 or BeF_2, BeO is not resistant to AlF_3, and Li_2O is not resistant to any of the fluorides.

The tabular data can also be represented graphically as in Figs. 25-30. In Fig. 25, for example we consider possible chemical equilibria of chlorides formed by reaction with a 33%Mg - 33%Li - 33%Al alloy. For the calculation, activities of Mg and Li metal are set equal to the mole fractions and Al is treated as a diluent while it is assumed that the activity of LiCl is 0.1, 0.5, or 0.9. We then calculate the ratio of the activities of $MgCl_2/LiCl$ as a function of temperature. The calculated

activity ratio varies from 10^{-14} to 10^{-7} showing that given this set of conditions and assuming thermodynamic equilibrium, essentially no $MgCl_2$ is formed until all of the Li has reacted to form LiCl. In Fig. 26 the same system is considered with regard to the chlorides of Mg and Al (Li is treated as a diluent); as indicated, the result that the $MgCl_2/AlCl_3$ ratio varies between 10^{-23} and 10^{-15}. Thus, the Li/Mg/Al alloy system would react with Cl_2 to form first LiCl followed by $MgCl_2$ and finally $AlCl_3(g)$. The results of similar calculations for fluoride reactions in this alloy system are shown in Fig. 27 and 28. Fig. 27 shows that LiF is formed preferentially over MgF_2 while Fig. 28 shows the preferential formation of LiF over AlF_3. Again, as with the chlorides, the order of fluorine reaction in a system at thermodynamic equilibrium would first consume all Li followed by Mg and finally Al. Figs. 29 and 30 demonstrate that LiF and MgF_2 will be formed in preference to LiCl and $MgCl_2$ even if $Cl_2(g)$ is present at much higher concentrations than $F_2(g)$.

To summarize, formation of oxides will be negligible in the presence of F_2 until all the fluorine has been used up. Next, oxides will form if thermodynamic equilibrium is achieved. Note that generally this is not what we have observed in laboratory studies but this probably means that the activation energy necessary to form the oxides is not achieved in the temperature region we are obtaining. Finally chlorides will be formed. However, note that the thermodynamic data predicts that only Li_2O will react with $Cl_2(g)$. Thus, these calculations suggest that there may be problems in obtaining relatively complete or uniform combustion.

D. Reactant/Product Vapor Pressures

It is necessary to consider vapor pressures of reactants or expected products formed in the various combustion systems. In the case of a Li/Al or Li/Mg alloy with which water is reacted, the Li in the condensed phase could absorb H_2 to form LiH. Fig. 31 shows the H_2 pressure over pure LiH(ℓ) based on data from the JANAF tables [5]. These data assume that both Li and LiH(ℓ) are pure phases. In reality Li dissolves to some extent in the LiH(ℓ) so that the pressure is actually less than this estimate. Note that the H_2 pressure is close to an atmosphere at 1200 K. The effect of a second alloying element might decrease this pressure and the Li activity might be decreased by as much as a factor of two. In spite of this, Li alloy at lower temperatures might absorb a significant fraction of the H_2 produced thus reducing the amount of H_2 available for reaction.

Fig. 32 shows that LiOH(g) could present a transport problem in reactions (1) and (2). Also it could be significant that the water pressure over LiOH at 1300K approaches one atm, raising the possibility of producing Li_2O, and thereby increasing the energy yield. By contrast, Fig. 33 indicates that the pressures of LiCl and LiF are to low to be relevant to transport processes by vaporization.

Data shown in Fig. 34 for the Al halides indicates that very high pressures could be established by $AlCl_3$(g). JANAF[5] reports a critical temperature of 620 K and a critical pressure of 24.3 atm. Our measurements show the formation of mixed halide vapors formed by the

reaction of ClO_3F with Al metal. JANAF tabulates data for some of the mixed halide species. This problem will receive further consideration in subsequent studies.

Fig. 35 shows the $BeCl_2$, Be_2Cl_4, and BeF_2 vapor pressure curves. As with $AlCl_3$, the vapor pressure of $BeCl_2$ will be very high at 1200 K. Estimates based on the JANAF[5] tabulation indicate a pressure of 90 atm at 1200 K.

In Fig. 36 vapor pressure data for Mg(g), and $MgCl_2$ are represented. The pressure of Mg(g) is about 0.2 atm at 1200 K.

V. DISCUSSION AND FUTURE DIRECTIONS

It is apparent that in dealing with the complex high temperature chemistry of the multicomponent kinetic processes occurring during the stored chemical energy release reactions discussed here, it is necessary to consider the reaction behavior of the component pairs individually (e.g., Al/F_2, Al/Cl_2, Al/O_2, Mg/F_2, Mg/Cl_2, etc.) In future studies, rate data will be collected as a function of temperature for these basic reactions.

Phase equilibria, especially melting, determine to a large degree the properties of reaction products. Phase equilibrium measurements will be initiated on the system Li-Mg-Al-O-F to explore further the possibility of oxy-fluoride phase formation.

A few comments concerning importance of vapor pressures in these propulsion systems should be made. In most of these systems where individual chloride and fluoride species are present, additional complex species each containing chlorine, fluorine and one or more metals may be formed leading to higher pressures than have been calculated here. The phenomenon of volatility enhancement by vapor complexing has been discussed in detail elsewhere [7]. Also, the temperature in the flame region of the device will likely be much higher than 1200 K leading to much higher pressures in the flame region. Since the walls of the device are cooler, condensation and vapor entrapment of fuel is a possible problem area. Hence, additional experiments are planned using high pressure transpiration mass spectrometry to identify the various species formed and to measure their partial pressures as well as to examine the role of kinetic factors in gas phase transport.

VI. REFERENCES

1. L. P. Cook, E. R. Plante, R. S. Roth, and J. W. Hastie, 1984, "Phase Equilibria of Stored Chemical Energy Reactants", National Bureau of Standards Report No. NBSIR 84-2940, 103 p. (1984).

2. L. P. Cook and E. R. Plante, 1985, "Survey of Alternate Stored Chemical Energy Reactions", National Bureau of Standards Report No. NBSIR 85-3282, 106 p. (1985).

3. M. C. Sneed, J. L. Maynard, and R. C. Brasted, "Inorganic Chemistry", D. Van Nostrand Company Inc., New York, N.Y., Vol. 3, p. 29 (1954).

4. A. Engelbrecht and H. Atzanger, Monatsh. 83, p. 1087 (1952).

5. JANAF Thermochemical Tables, 2nd Ed., NSRDS-NBS 37, Washington, D.C. (1971).

6. D. W. Bonnell and J. W. Hastie, Transpiration Mass Spectrometry of High Temperature Vapors, p 357, in "Characterization of High Temperature Vapors and Gases", J. W. Hastie, ed.; NBS SP 561/1 and 2, U.S. Govt. Printing Office, Washington, D.C. (1979).

7. J. W. Hastie, "High Temperature Vapors", Acad. Press, New York, p. 480 (1975).

Table 1. Thermodynamically Predicted Product Phases for SCEPS Reactions

Reaction	Predicted Products (initial stage or stages)
(1) Li/H_2O, H_2/O_2	LiOH, H_2
(2) Li/H_2O, NaO_2/H_2O, H_2/O_2	LiOH, H_2, NaOH, O_2
(3) $MgAl/H_2O$, H_2/O_2	MgO, $MgAl_2O_4$, H_2
(4) $LiAl/ClO_3F$	Al_2O_3, LiF, LiCl
(5) $LiAlMg/ClO_3F$	MgF_2, LiF, LiCl, $MgAl_2O_4$, MgO
(6) $LiBe/ClO_3F$	BeO, Li_2O, LiF, LiCl
(7) $Li/C_{11}F_{20}$	C, LiF
(8) LiB/NF_3	LiF, BN

Table 2. Experimental Test of Thermodynamically Predicted SCEPS Product Phases

Reaction	Starting Materials	Temp. (°C)	Time (hr)	X-ray Analysis of Results
(4)	LiF,LiCl,Al_2O_3	600	48	LiCl, LiCl H_2O*, Al_2O_3, LiF
(4)	LiF,LiCl,Al_2O_3	800	23	LiCl, LiCl H_2O*, Al_2O_3, LiF
(4)	LiF,LiCl,Al_2O_3	1000	23	LiCl, LiF, $LiAl_5O_8$
(4)	LiF,LiCl,Al_2O_3	1200	116 (quenched)	LiCl, LiCl H_2O* LiF, $LiAl_5O_8$
(7)	LiF,C	1200	24	LiF, C
(8)	LiF,BN	600	18	LiF, BN
(8)	LiF,BN	800	24	LiF, BN
(8)	LiF,BN	1000	22	LiF, BN

*hydration upon atmospheric exposure

Table 3. Possibilities for Enhanced Local Transport of Li, Mg

A. Metal vaporization

(1) $Li(\ell) \rightarrow Li(g)$

(2) $2\ Li(g) + F_2(g) \rightarrow 2\ LiF(c)$

(3) $Mg(\ell) \rightarrow Mg(g)$

(4) $Mg(g) + F_2(g) \rightarrow MgF_2(c)$

B. Metastable formation of chloride species

(1) $2\ Li(\ell) + Cl_2(g) \rightarrow 2\ LiCl(g)$

(2) $2\ LiCl(g) + F_2(g) \rightarrow 2\ LiF(c) + Cl_2(g)$

(3) $Mg(\ell) + Cl_2(g) \rightarrow MgCl_2(g)$

(4) $MgCl_2(g) + F_2(g) \rightarrow MgF_2(c) + Cl_2(g)$

C. Combined mechanism

(1) $Li(\ell) \rightarrow Li(g)$

(2) $2\ Li(g) + Cl_2(g) \rightarrow LiCl(g)$

(3) $2\ LiCl(g) + F_2(g) \rightarrow 2\ LiF(c)$

(4) $Mg(\ell) \rightarrow Mg(g)$

(5) $Mg(g) + Cl_2(g) \rightarrow MgCl_2(g)$

(6) $MgCl_2(g) + F_2(g) \rightarrow MgF_2(c)$

Table 4. Weight Gain of 0.3 μm Alumina as a Function of Temperature in Flowing ClO_3F (nominal flow rate of 1 sccm)

Temp. (°C)	Time (hr)	Initial Wt. (mg)	Wt. Gain (mg)	% Wt. Gain	Reaction End Point	% of Theoretical Max.
450	1.5	116.6	18.3	15.7	N	24.3
500	1.5	119.2	34.8	29.2	N	45.1
550	1.5	91.7	47.1	51.4	N	79.4
600	0.9	95.4	53.4	56.0	Y	86.5
690	1.4	94.6	55.8	59.0	Y	91.2
700	1.3	78.9	47.6	60.3	Y	93.2
750	1.3	77.3	48.7	63.0	Y	97.3
800	1.4	95.1	59.5	62.6	Y	96.7

Table 5. Effect of ClO_3F Flow Rate on Reaction with 0.3 μm Alumina at 800°C

Approx. Flow Rate (sccm)	Time to Reaction End Point (hr)	Initial Wt. (mg)	Wt. Gain (mg)	% Wt. Gain	% of Theoretical Max.
1	1.1	64.2	39.0	60.75	93.87
3	1.0	129.8	78.6	60.55	93.56
5	0.4	81.3	49.6	61.01	94.27

Table 6. Calculated Rate Constants for Parabolic Portion of Al_2O_3/ClO_3F Reaction Data

Temp (°C)	Flow Rate (sccm)	Parabolic Rate Constant ($mg/m^2.s$)
450	1	0.008
500	1	0.003
550	1	0.113
600	1	0.358
650	1	0.517
700	1	0.573
750	1	0.607
800	1	0.584
800	0.7	0.660
800	3	0.711
800	5	2.390

Table 7. Weight Gain of Liquid Al Droplets as a Function of Temperature in Flowing ClO_3F (nominal flow rate of 1 sccm)

Temp. (°C)	Time (hr)	Initial Wt. (mg)	Calc. Surface Area (cm^2)	Wt. Gain (mg)	Calc. Thickness of Reaction Layer (μm)*
700	0.3	420.0	1.52	0.34	2
750	0.3	413.6	1.51	0.76	3
800	0.8	418.2	1.52	2.75	10

*Assumes uniform coverage of AlF_3.

Table 8. Effect of ClO_3F Flow Rate on Reaction with Liquid Al Droplets at 800°C

Approx. Flow Rate (sccm)	Time (hr)	Initial Wt. (mg)	Calc. Surface Area (cm^2)	Wt. Gain (mg)	Calc. Thickness of Reaction Layer (μm)*
0.7	0.3	411.6	1.50	1.9	7
2.0	0.3	412.1	1.50	1.7	6
5.0	0.2	417.9	1.52	1.8	7

*Assumes uniform coverage of AlF_3.

Table 9. Calculated Rate Constants for Parabolic Portion of Al/ClO_3F Reaction Data

Temp (°C)	Nominal ClO_3F Flow Rate (cc/min)	Parabolic Rate Constant ($mg/m^2.s$)
700	1	27
750	1	155
800	1	149
800	0.7	1340
800	3	1260
800	6	2210

Table 10. Mass Spectral Ion Intensities in the System ClO_3F - Al at 725°C

Mass (μ)	Species	Intensity (microvolts)
32	O_2	6200
46	AlF^+	~5
62	$AlCl^+$	140
65	AlF_2^+	50
70	Cl_2^+	6600
81	$AlClF^+$	110
85	SiF_3^+	1500
100	AlF_2Cl^+	55
116	$AlCl_2F^+$	78
132	$AlCl_3^+$	300

Table 11. Interactions of Chlorides and Fluorides

A. Exchange Reactions

(1) $2\ Al(\ell) + 3\ BeCl_2(g) = 3\ Be(c) = 2\ AlCl(g)$

(2) $2\ Al(\ell) + 3\ BeF_2(\ell) = 3\ Be(c) + 2\ AlF_3(\ell)$

(3) $Al(\ell) + 3\ LiCl(\ell) = Li(\ell) + AlCl_3(g)$

(4) $Al(\ell) + 3\ MgCl_2(\ell) = 3\ Li(\ell) + AlF_3(\ell)$

(5) $2Al(\ell) + 3\ MgCl_2(\ell) = 3\ Mg(\ell) + 2\ AlCl_3(g)$

(6) $2\ Al(\ell) + 3\ MgF_2(\ell) = 2\ AlF_3(\ell) + Mg(\ell)$

(7) $2\ Li(\ell) + BeCl_2(g) = Be(c) + 2\ LiCl(\ell)$

(8) $2\ Li(\ell) + BeF_2(c) = Be(c) + 2\ LiF(\ell)$

(9) $2\ Li(\ell) + MgCl_2(\ell) = Mg(\ell) + 2\ LiCl(\ell)$

(10) $2\ Li(\ell) + MgF_2(\ell) = Mg(\ell) + 2\ LiF(\ell)$

(11) $Mg(\ell) + BeCl_2(g) = Be(c) + MgCl_2(\ell)$

(12) $Mg(\ell) + BeF_2(\ell) = Be(c) + MgF_2(\ell)$

B. Gibbs Free Energies of Reaction (Calories)

	Temperature (K)					
Reaction	800	900	1000	1100	1200	1300
(1)	8,101	12,428	16,774	21,104	25,449	29,759
(2)	53,692	54,383	55,163	56,044	56,988	58,031
(3)	113,793	111,162	108,703	106,351	104,137	102,007
(4)	84,883	84,984	85,193	85,498	85,858	86,315
(5)	101,498	96,053	96,817	96,760	80,862	76,102
(6)	94,960	95,485	96,028	96,617	97,296	98,057
(7)	-73,162	-69,965	-66,877	-63,866	-60,942	-58,085
(8)	-40,705	-40,046	-39,556	-39,185	-38,909	-38,691
(9)	-42,030	-42,090	-42,196	-42,314	-42,471	-42,637
(10)	-24,935	-24,828	-24,786	-24,793	-24,807	-24,858
(11)	-31,132	-27,875	-24,681	-21,552	-18,471	-15,448
(12)	-13,756	-13,701	-13,622	-13,524	-13,436	-13,342

C. Summary of Stabilities at 1300 K (x = stable)

	$AlCl_3$	AlF_3	$BeCl_2$	BeF_2	$MgCl_2$	MgF_2	LiCl	LiF
Al	X	X	X	X	X	X	X	X
Be	O	O	X	X	X	X	X	X
Mg	O	O	O	O	X	X	X	X
Li	O	O	O	O	O	O	X	X

Table 12. Interaction of Oxides with Fluorine or Chlorine

A. Exchange Reactions

(1) $2\ Al_2O_3(c) + 12\ F_2(g) = AlF_3(c) + 3\ O_2(g)$

(2) $2\ BeO(c) + 2\ F_2(c) = BeF_2(g) + O_2(g)$

(3) $2\ Li_2O(c) + 2\ F_2(g) = 4\ LiF(\ell) + O_2(g)$

(4) $2\ MgO(c) + 2\ F_2(g) = 2\ MgF_2(\ell) + O_2(g)$

(5) $2\ Al_2O_3(c) + 6\ Cl_2(g) = 4\ AlCl_3(g) + 3\ O_2(g)$

(6) $2\ BeO(c) + 2\ Cl_2(g) = 2\ BeCl_2(g) + O_2(g)$

(7) $2\ Li_2O(c) + 2\ Cl_2(g) = 4\ LiCl(\ell) + O_2(g)$

(8) $2\ MgO(c) + 2\ Cl_2(g) = 2\ MgCl_2(\ell) + O_2(g)$

B. Gibbs Free Energies of Reaction (Calories)

	Temperature (K)					
Reaction	800	900	1000	1100	1200	1300
(1)	-562,682	-553,481	-544,387	-535,387	-526,461	-517,607
(2)	-132,802	-138,020	-143,180	-148,287	-153,345	-158,379
(3)	-272,435	-271,964	-271,635	-271,428	-271,285	-271,230
(4)	-212,096	-210,745	-209,444	-208,202	-207,077	-206,048
(5)	160,087	150,226	140,453	130,782	121,224	111,744
(6)	73,510	67,981	62,494	57,056	51,657	46,290
(7)	-89,689	-90,819	-92,107	-93,476	-94,946	-96,445
(8)	4,839	4,925	4,905	4,792	4,590	4,295

C. Summary of Stabilities at 1300 K (x = stable)

	F	Cl
Al_2O_3	O	X
BeO	O	X
MgO	O	X
Li_2O	O	O

Table 13. Reaction of Chlorides with Fluorine

A. Exchange Reactions

(1) $2\ AlCl_3(g) + 3\ F_2(g) = 2\ AlF_3(\ell) + Cl_2(g)$

(2) $BeCl_2(g) + F_2(g) = BeF_2(\ell) + Cl_2(g)$

(3) $2\ LiCl(\ell) + F_2(g) = 2\ LiF(\ell) + Cl_2(g)$

(4) $MgCl_2(\ell) + F_2(g) = MgF_2(\ell) + Cl_2(g)$

B. Gibbs Free Energies of Reaction (Calories)

	Temperature (K)					
Reaction	800	900	1000	1100	1200	1300
(1)	-331,940	-324,073	-316,311	-308,633	-301,067	-293,560
(2)	-125,844	-122,009	-118,234	-114,525	-110,869	-107,277
(3)	-91,373	-90,572	-89,764	-88,976	-88,170	-87,392
(4)	-108,467	-107,835	-107,174	-106,497	-105,834	-105,172

C. Summary of Stabilities at 1300K (0 = unstable)

	F
$AlCl_3$	0
$BeCl_2$	0
LiCl	0
$MgCl_2$	0

Table 14. Interaction of Chlorides with Fluorides

A. Exchange Reactions

(1) $2\ AlF_3(\ell) + 3\ BeCl_2(g) = 2\ AlCl_3(g) + 3\ BeF_2(\ell)$

(2) $AlF_3(\ell) + 3\ LiCl(\ell) = AlCl_3(g) + 3\ LiF(\ell)$

(3) $2\ AlF_3(\ell) + 3\ MgCl_2(\ell) = 2\ AlCl_3(g) + 3\ MgF_2(\ell)$

(4) $BeF_2(\ell) + 2\ LiCl(\ell) = BeCl_2(g) + 2\ LiF(\ell)$

(5) $BeF_2(\ell) + MgCl_2(\ell) - BeCl_2(g) + MgF_2(\ell)$

(6) $2\ LiF(\ell) + MgCl_2(\ell) = 2\ LiCl(\ell) + MgF_2(\ell)$

B. Gibbs Free Energies of Reaction (Calories)

	Temperature (K)					
Reaction	800	900	1000	1100	1200	1300
(1)	-45,591	-41,955	-38,509	-34,940	-31,539	-28,272
(2)	28,910	26,178	23,509	20,852	18,279	15,692
(3)	6,538	0,568	-5,212	-10,857	-16,434	-21,955
(4)	34,471	31,437	28,469	25,548	22,699	19,885
(5)	17,376	14,174	11,059	8,028	5,035	2,106
(6)	-17,094	-17,263	-17,410	-17,520	-17,664	-17,779

C. Summary of Stabilities at 1300K (x = stable)

	AlF_3	BeF_2	MgF_2	LiF
$AlCl_3$	X	X	X	0
$BeCl_2$	X	X	0	0
$MgCl_2$	0	X	X	0
LiCl	X	X	X	X

Table 15. Interaction of Oxides with Fluorides

A. Exchange Reaction

(1) $Al_2O_3(c) + 3\ BeF_2(\ell) = 2\ AlF_3(\ell) + 3\ BeO(c)$

(2) $Al_2O_3(c) + 6\ LiF(\ell) = 2\ AlF_3(\ell) + 3\ Li_2O(c)$

(3) $Al_2O_3(c) + 3\ MgF_2(\ell) = 2\ AlF_3(\ell) + 3\ MgO(c)$

(4) $BeO(c) + 2\ LiF(\ell) = BeF_2(\ell) + Li_2O(c)$

(5) $BeO(c) + MgF_2(\ell) = BeF_2(\ell) + MgO(c)$

(6) $Li_2O(c) + MgF_2(\ell) = 2\ LiF(\ell) + MgO(c)$

B. Gibbs Free Energies of Reaction (Calories)

	Temperature (K)					
Reaction	800	900	1000	1100	1200	1300
(1)	15,370	15,097	14,875	14,747	14,666	14,710
(2)	156,756	158,985	161,368	163,900	166,473	169,157
(3)	66,247	67,157	68,080	69,060	70,160	71,385
(4)	47,129	47,963	48,831	49,718	50,602	51,482
(5)	16,959	17,353	17,735	18,104	18,498	18,892
(6)	-30,170	-30,609	-31,096	-31,613	-32,104	-32,591

C. Summary of Stabilities at 1300K (x = stable)

	AlF_3	BeF_2	MgF_2	LiF
Al_2O_3	X	X	X	X
BeO	O	X	X	X
MgO	O	O	X	X
Li_2O	O	O	O	X

Table 16. Interaction of Oxides with Chlorides

A. Exchange Reactions

(1) $Al_2O_3(c) + 3\ BeCl_2(c) = 2\ AlCl_3(c) + 3\ BeO(c)$

(2) $Al_2O_3(c) + 6\ LiCl(\ell) = 2\ AlCl_3(c) + 3\ Li_2O(c)$

(3) $Al_2O_3(c) + 3\ MgCl_2(\ell) = 2\ AlCl_3(c) + 3\ MgO(c)$

(4) $BeO(c) + 2\ LiCl(\ell) = BeCl_2(c) + Li_2O(c)$

(5) $BeO(c) + MgCl_2(\ell) = BeCl_2(c) + MgO(c)$

(6) $Li_2O(c) + MgCl_2(\ell) = 2\ LiCl(\ell) + MgO(c)$

B. Gibbs Free Energies of Reaction (Calories)

	Temperature (K)					
Reaction	800	900	1000	1100	1200	1300
(1)	-30,221	-26,858	-23,514	-20,193	-16,873	-13,562
(2)	214,577	211,342	208,387	205,605	203,030	200,540
(3)	72,785	67,725	62,869	58,203	53,727	49,430
(4)	81,599	79,400	77,300	75,266	73,301	71,367
(5)	34,335	31,528	28,794	26,132	23,533	20,997
(6)	-47,264	-47,872	-48,506	-49,134	-49,768	-50,370

C. Summary of Stabilities at 1300K (x = stable)

	$AlCl_3$	$BeCl_2$	$MgCl_2$	LiCl
Al_2O_3	X	O	X	X
BeO	X	X	X	X
MgO	O	O	X	X
Li_2O	O	O	O	X

VIII. FIGURES

Figure 1. Knudsen effusion mass spectrometric data for thermal decomposition of ClO_3F.

Figure 2. Schematic of high pressure transpiration mass spectrometer cell.

Figure 3. High pressure transpiration mass spectrometer data for thermal decomposition of ClO_3F.

Figure 4. Total pressure in high pressure transpiration mass spectrometer system as a function of temperature. Break in slope indicates beginning of ClO_3F decomposition.

Figure 5. Ion current data for $^{35}ClO_3^+$ in ClO_3F/transpiration mass spectrometer experiment of Figs. 3, 4.

Figure 6. Thermogravimetric curve for fluorine saturation of alumina cell by ClO_3F at 800°C.

Figure 7. Thermogravimetric data for reaction of 0.3 μm alumina powder with Clo_3F at various temperatures.

Figure 8. Thermogravimetric data for effect of ClO_3F flow rate on 0.3 μm alumina reaction at 800°C.

Figure 9. Plot of rate constants for ClO_3F/Al_2O_3 reaction data of Figs. 7 and 8.

Figure 10. Thermogravimetric data for fluorine saturation of MgO cell by ClO_3F at 800°C.

Figure 11. Melted aluminum ball of type used in reaction rate studies.

Figure 12. Surface of aluminum ball after reaction with ClO_3F at 800°C.

Figure 13. Surface of aluminum ball after ClO_3F reaction, showing surface channel under gas jet.

Figure 14. Thermogravimetric data for reaction of molten aluminum ball with ClO_3F at various temperatures.

Figure 15. Thermogravimetric data for effect of ClO_3F flow rate on aluminum reaction at 800°C.

Figure 16. Cooling curve for tungsten furnace used in Li_2O-Al_2O_3 phase equilibrium experiments.

Figure 17. Equilibrium crystals of $LiAl_5O_8$ spinel with recrystallized interstitial eutectic melt.

Figure 18. Phase diagram for the high alumina portion of the system $LiAlO_2$-Al_2O_3.

Figure 19. Lamellar intergrowths in $(Li_2O)_{2.5}$ $(Al_2O_3)_{97.5}$ cooled from 1925°C.

Figure 20. DTA analysis of phase transition in $LiAl_5O_8$.

Figure 25. Chemical equilibria of chlorides formed by reaction with LiMgAl alloy.

Figure 26. Chemical equilibria of (Mg,Al) chlorides formed by reaction with LiMgAl alloy.

Figure 27. Chemical equilibria of (Li, Mg) fluorides formed by reaction with LiMgAl alloy.

Figure 28. Chemical equilibria of (Li,Al) fluorides formed by reaction with LiMgAl alloy.

Figure 29. Partitioning of fluorine in the lithium molten salt phase.

Figure 30. Partitioning of fluorine in the magnesium molten salt phase.

Figure 31. Vapor pressure over molten lithium and over Li + LiH mixture.

Figure 32. Vapor pressures over LiOH and over LiOH + Li_2O mixture.

Figure 33. Partial pressures of Lithium species over their respective condensed phases.

Figure 34. Partial pressures of aluminum species over their respective condensed phases.

Figure 35. Partial pressures of beryllium species over their respective condensed phases.

Figure 36. Partial pressures of magnesium species over their respective condensed phases.

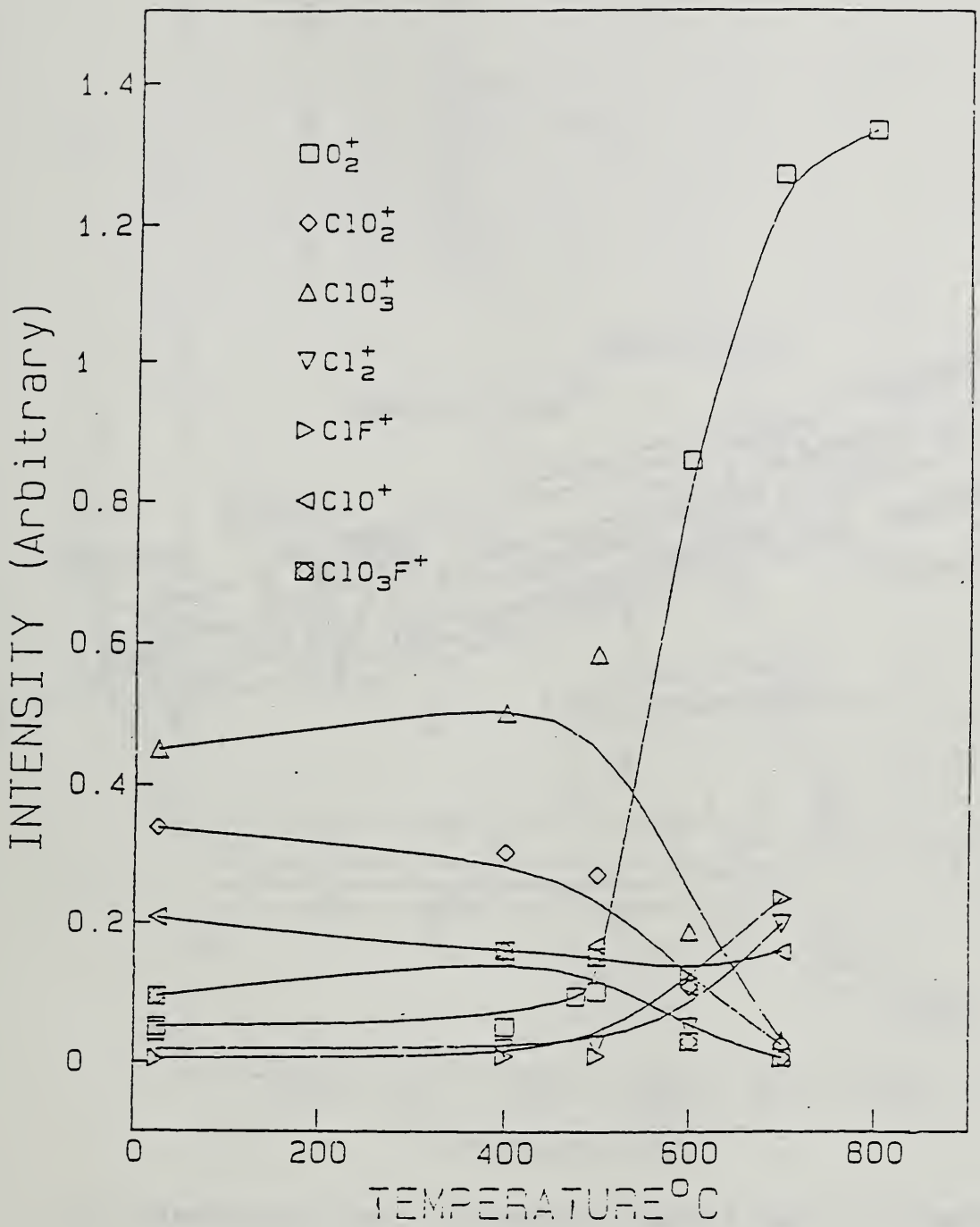

Figure 1. Knudsen effusion mass spectrometric ion intensity data for thermal decomposition of ClO_3F.

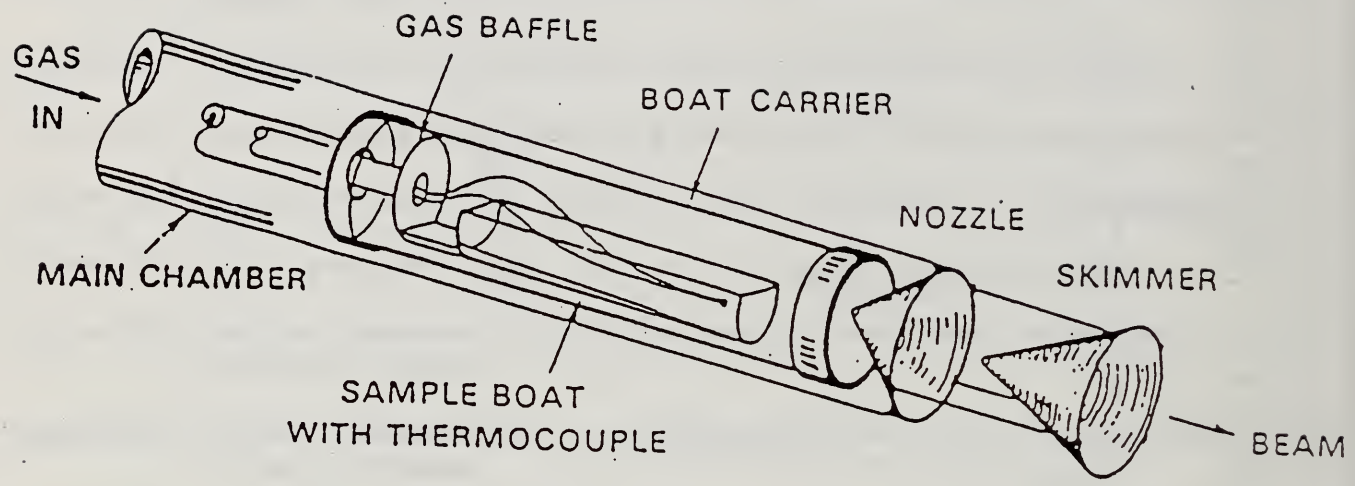

Figure 2. Schematic of high pressure transpiration mass spectrometer cell.

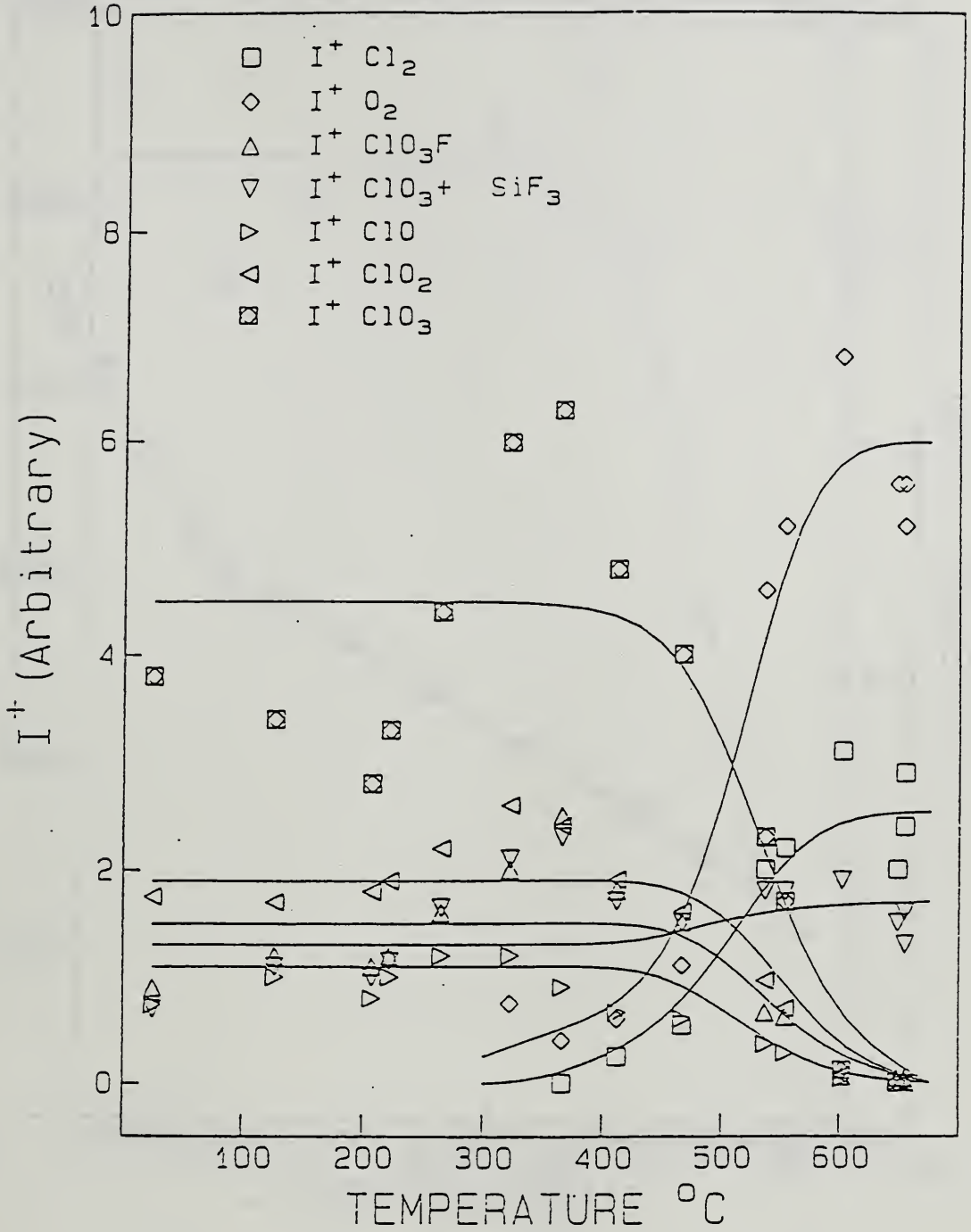

Figure 3. High pressure transpiration mass spectrometer ion intensity data for thermal decomposition of ClO_3F.

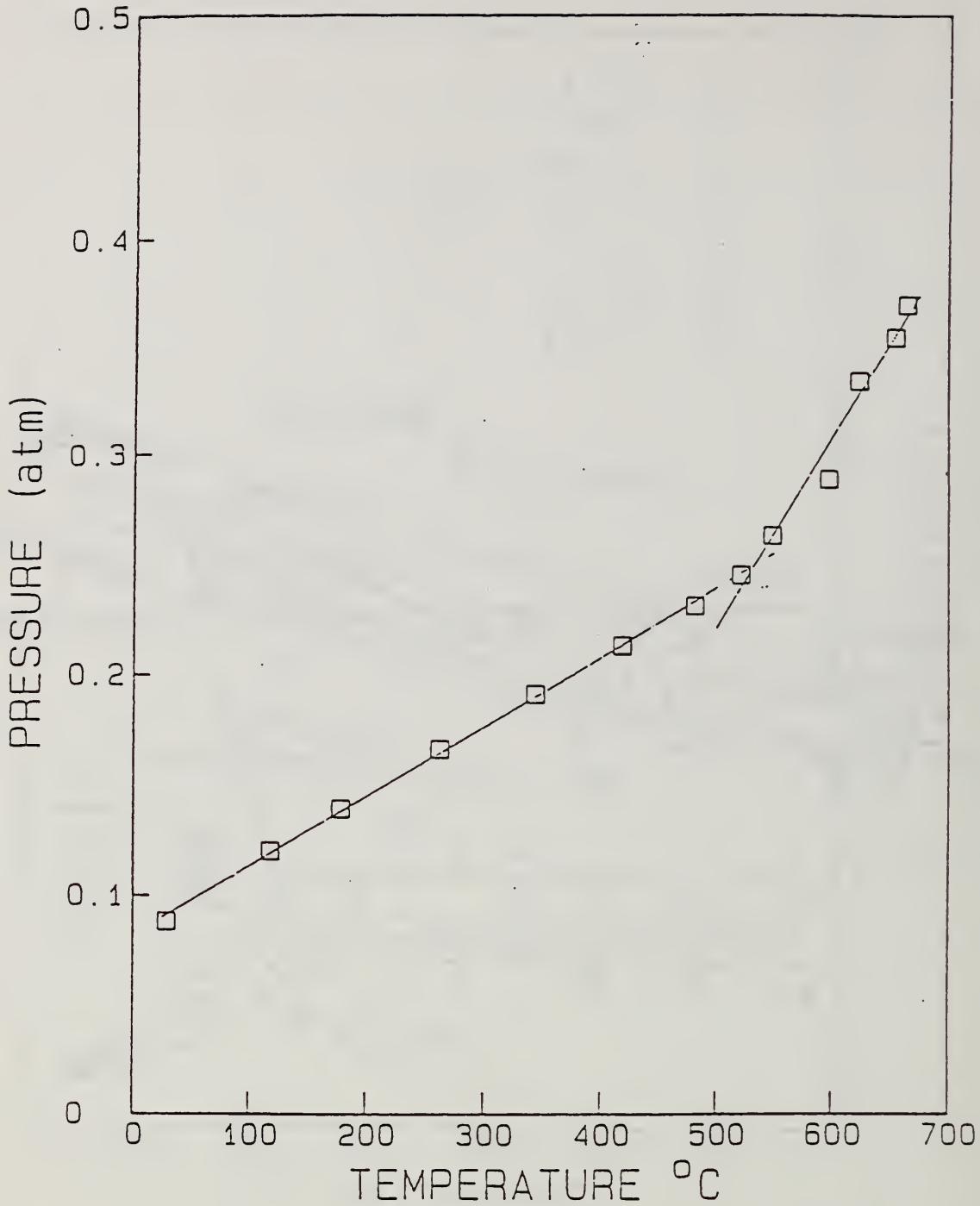

Figure 4. Total pressure in high pressure transpiration mass spectrometer system as a function of temperature. Break in slope indicates beginning of ClO_3F decomposition.

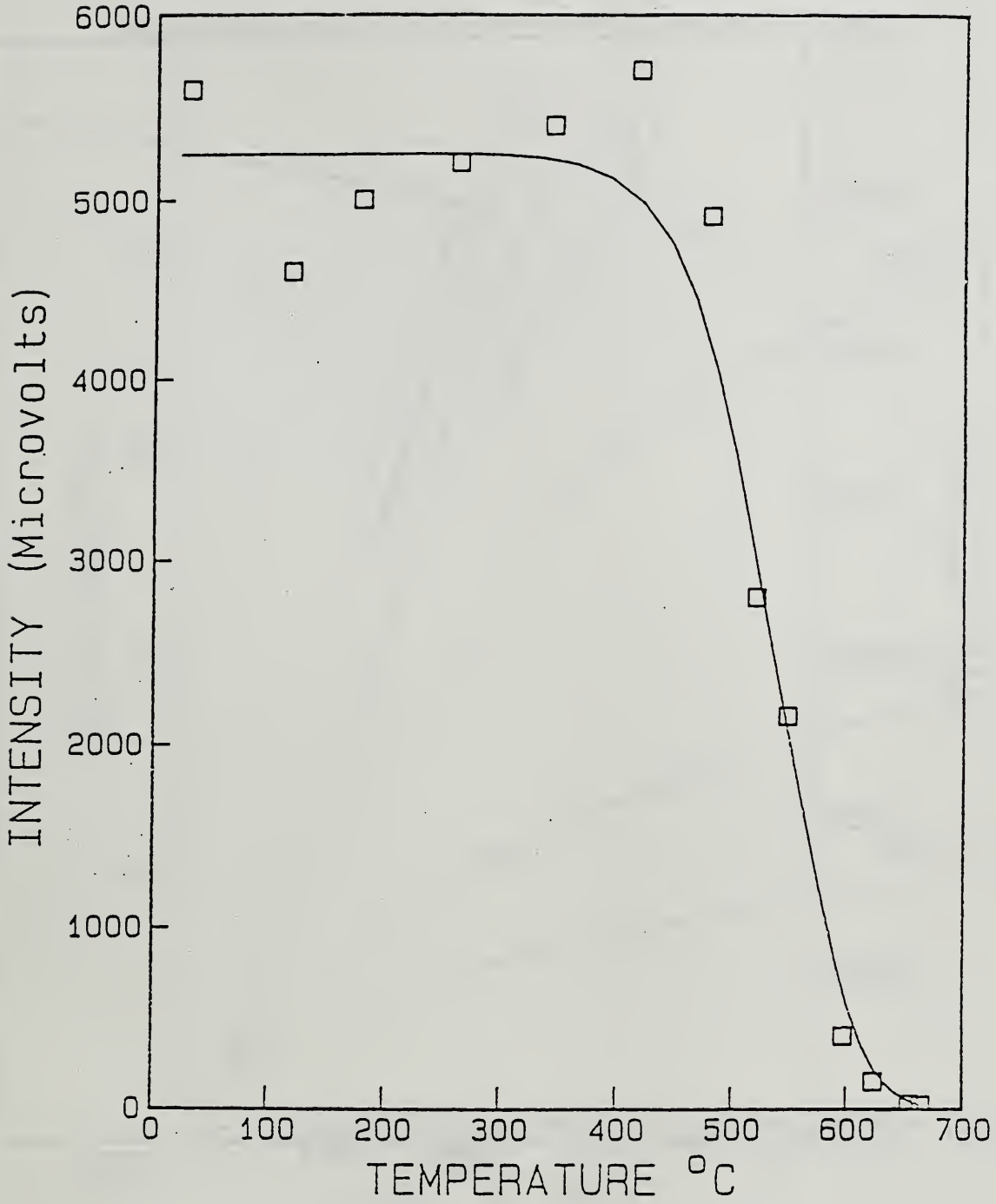

Figure 5. Ion current data for $^{35}ClO_3^+$ in ClO_3F/transpiration mass spectrometer experiment of Figs. 3, 4.

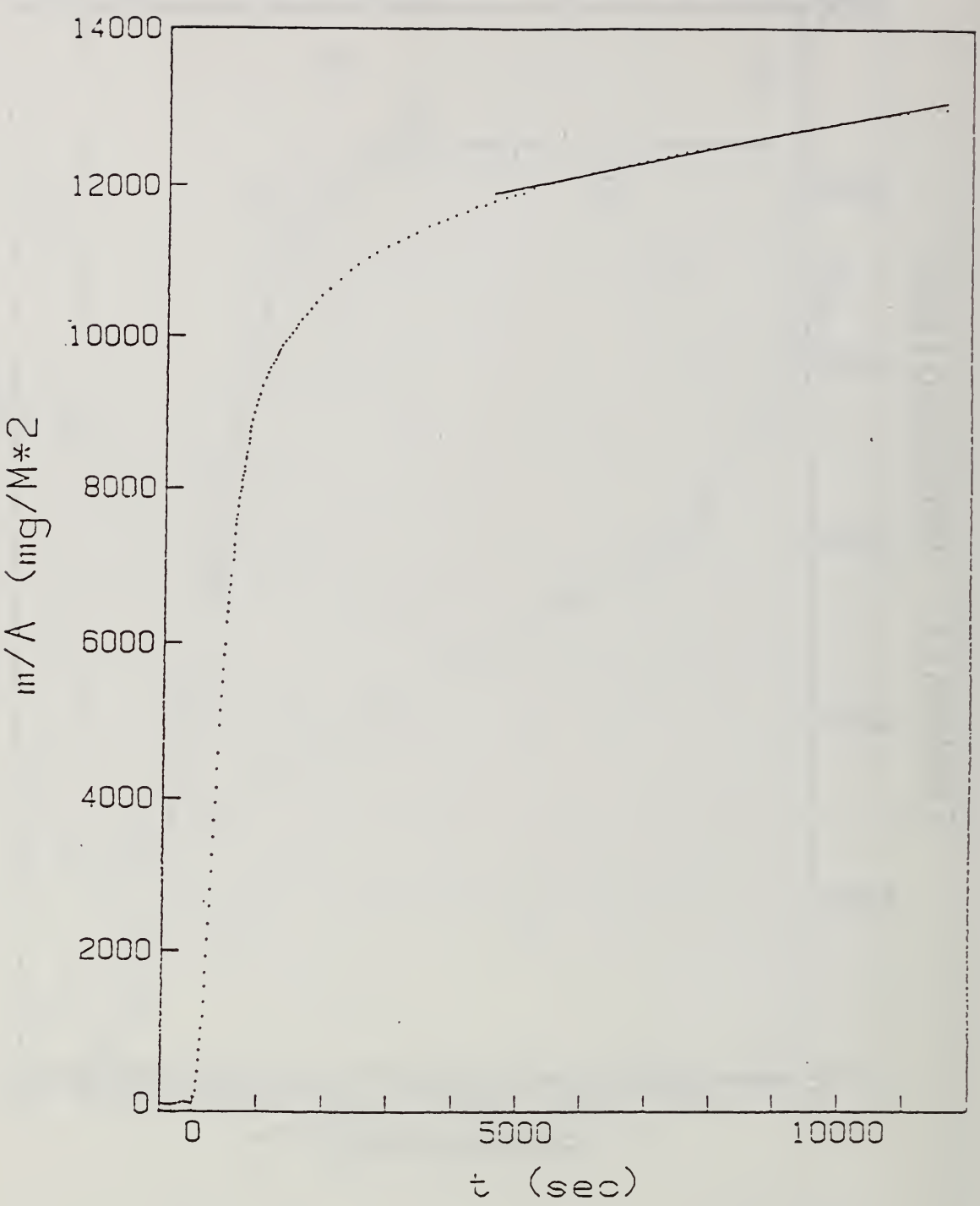

Figure 6. Thermogravimetric curve for fluorine saturation of alumina cell by ClO_3F at 800°C.

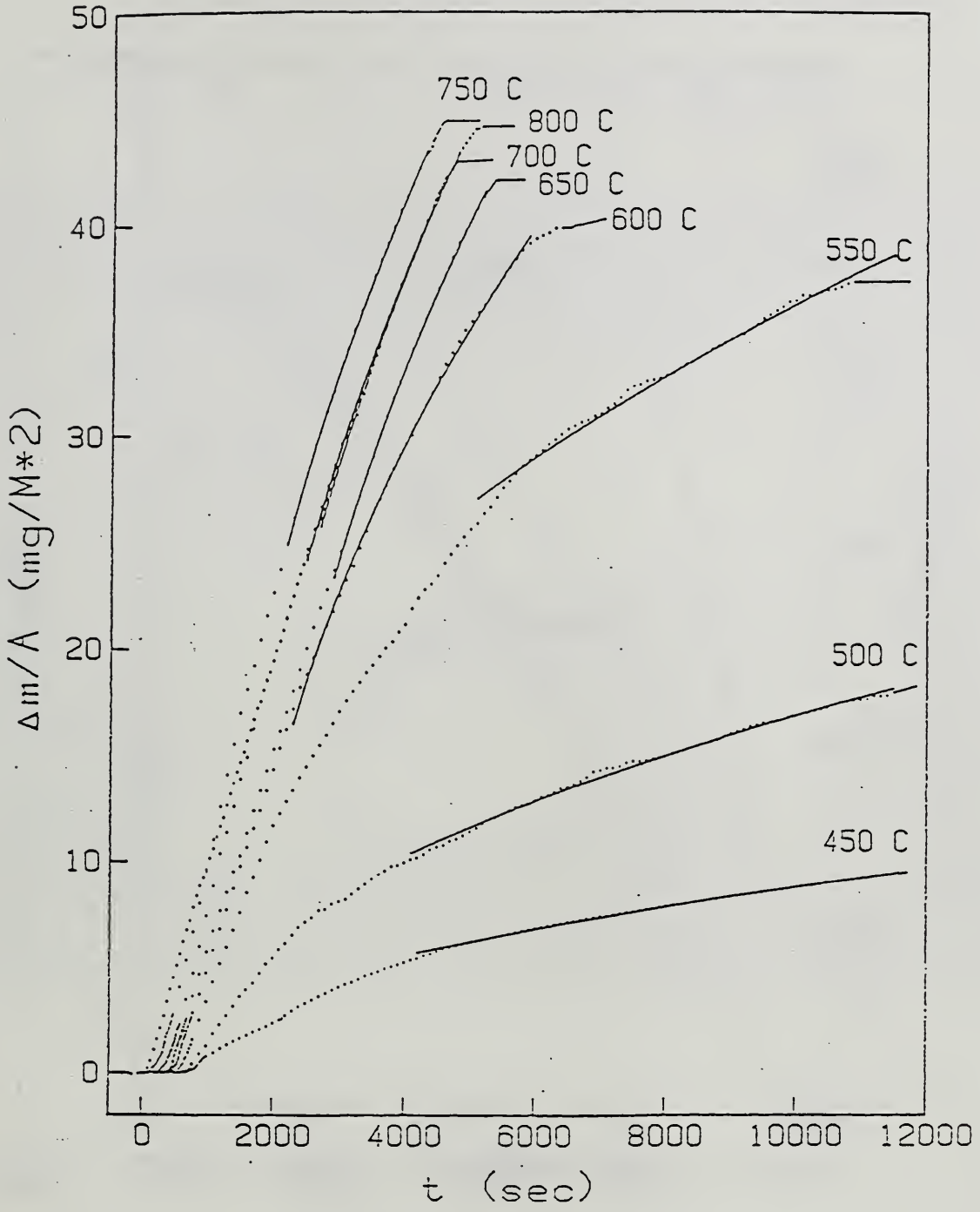

Figure 7. Thermogravimetric data for reaction of 0.3 μm alumina powder with ClO_3F at various temperatures.

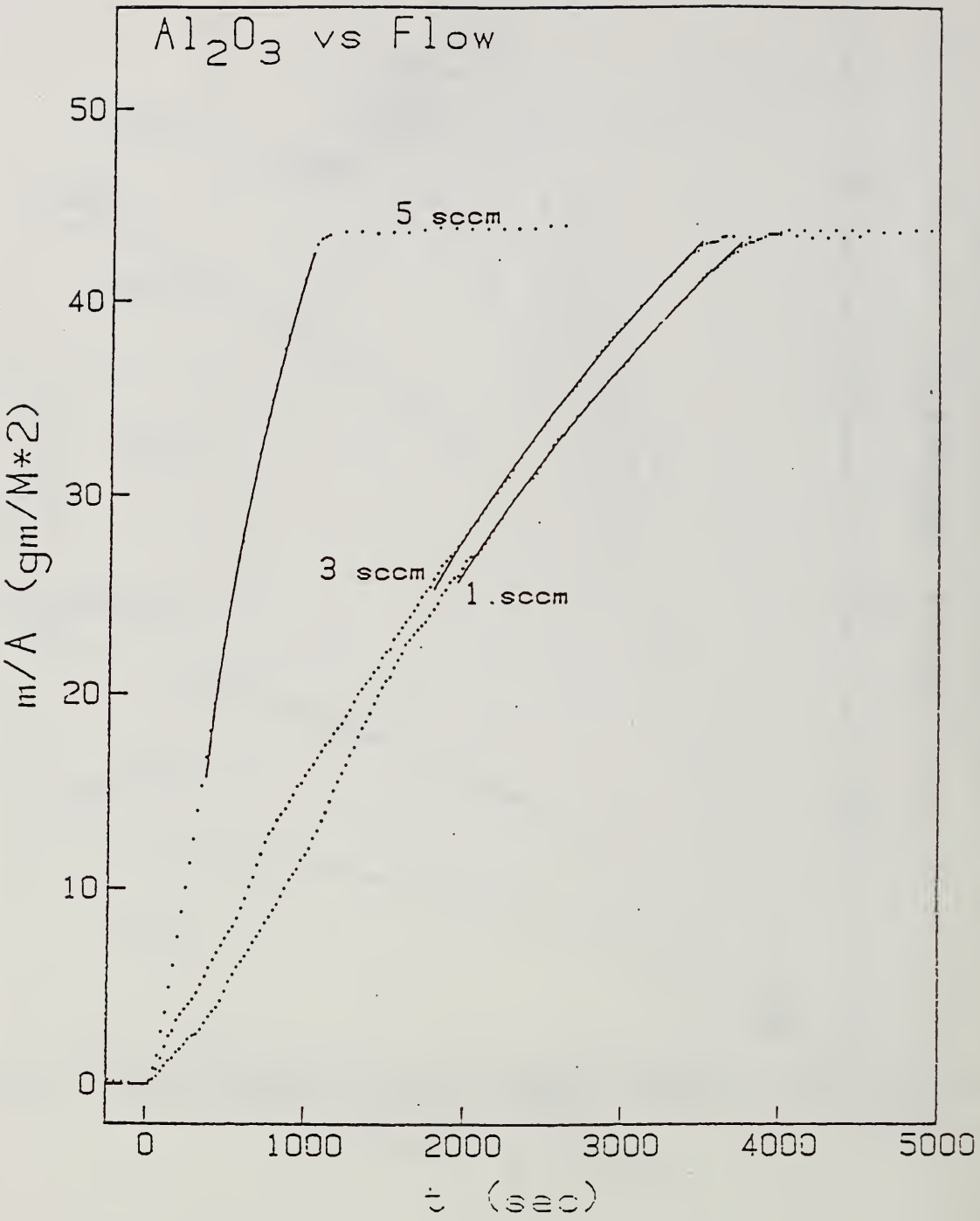

Figure 8. Thermogravimetric data for effect of ClO_3F flow rate on its reaction with 0.3 μm alumina at 800°C.

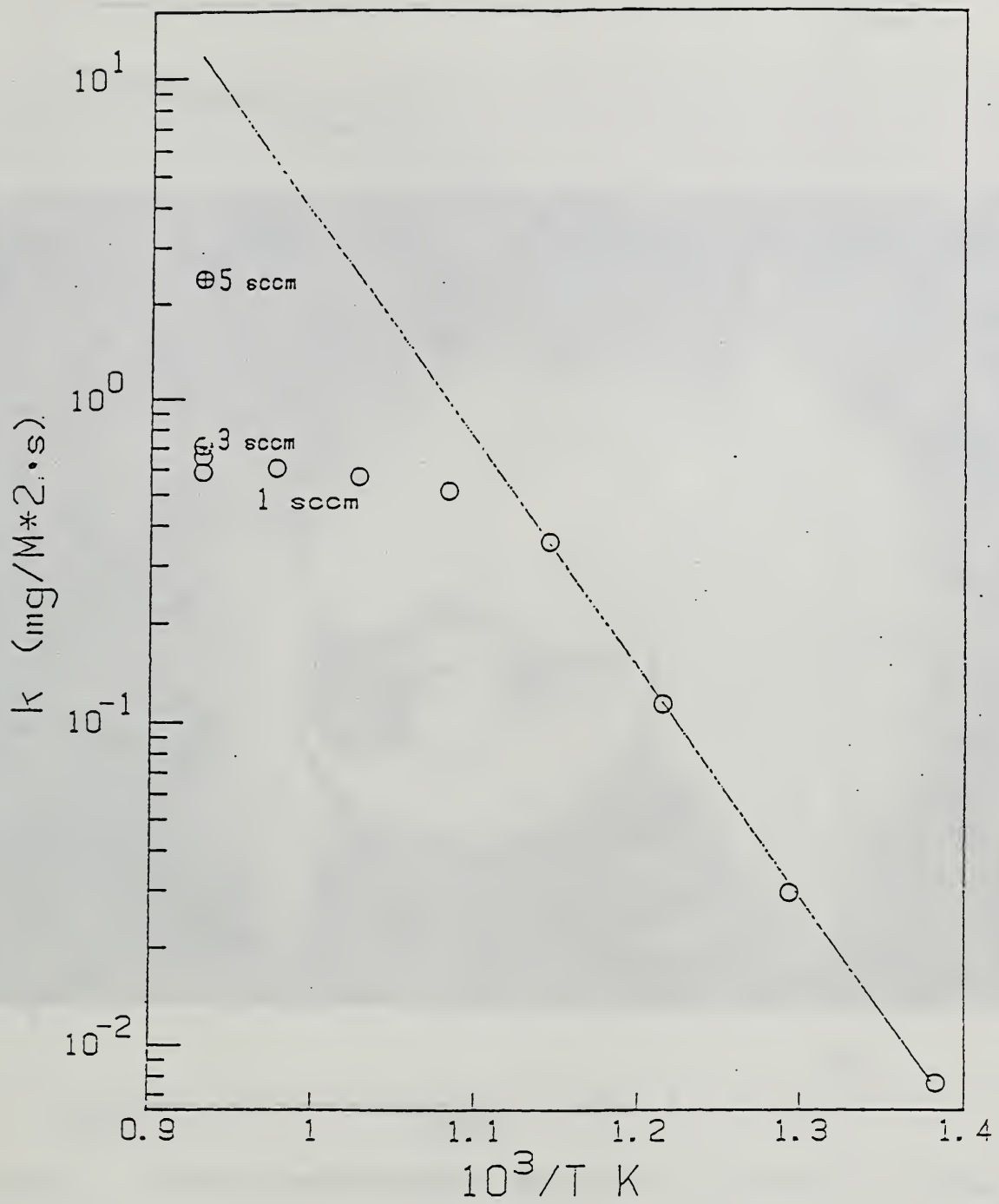

Figure 9. Rate constants for ClO_3F/Al_2O_3 reaction data of Figs. 7 and 8.

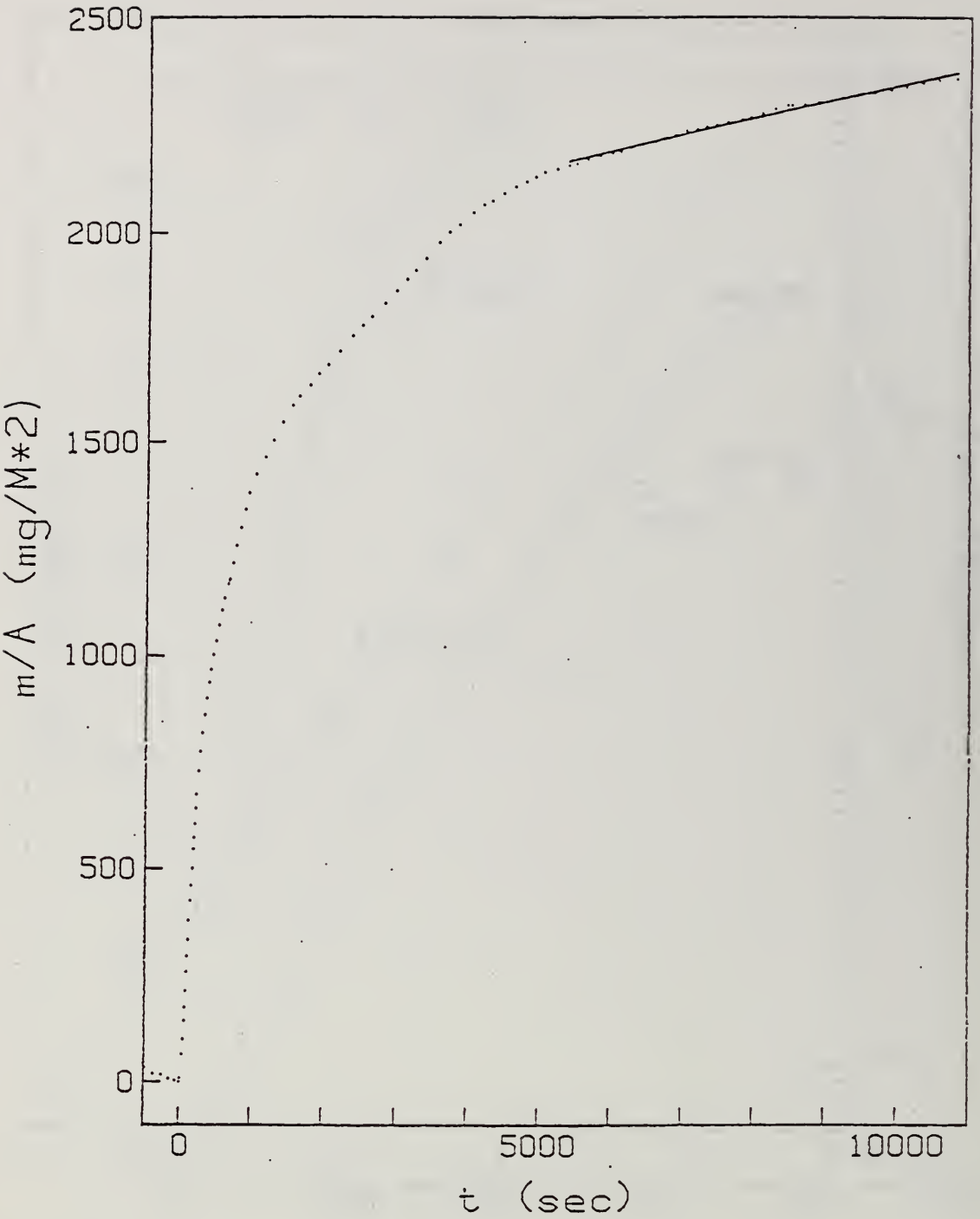

Figure 10. Thermogravimetric data for fluorine saturation of MgO cell by ClO_3F at 800°C.

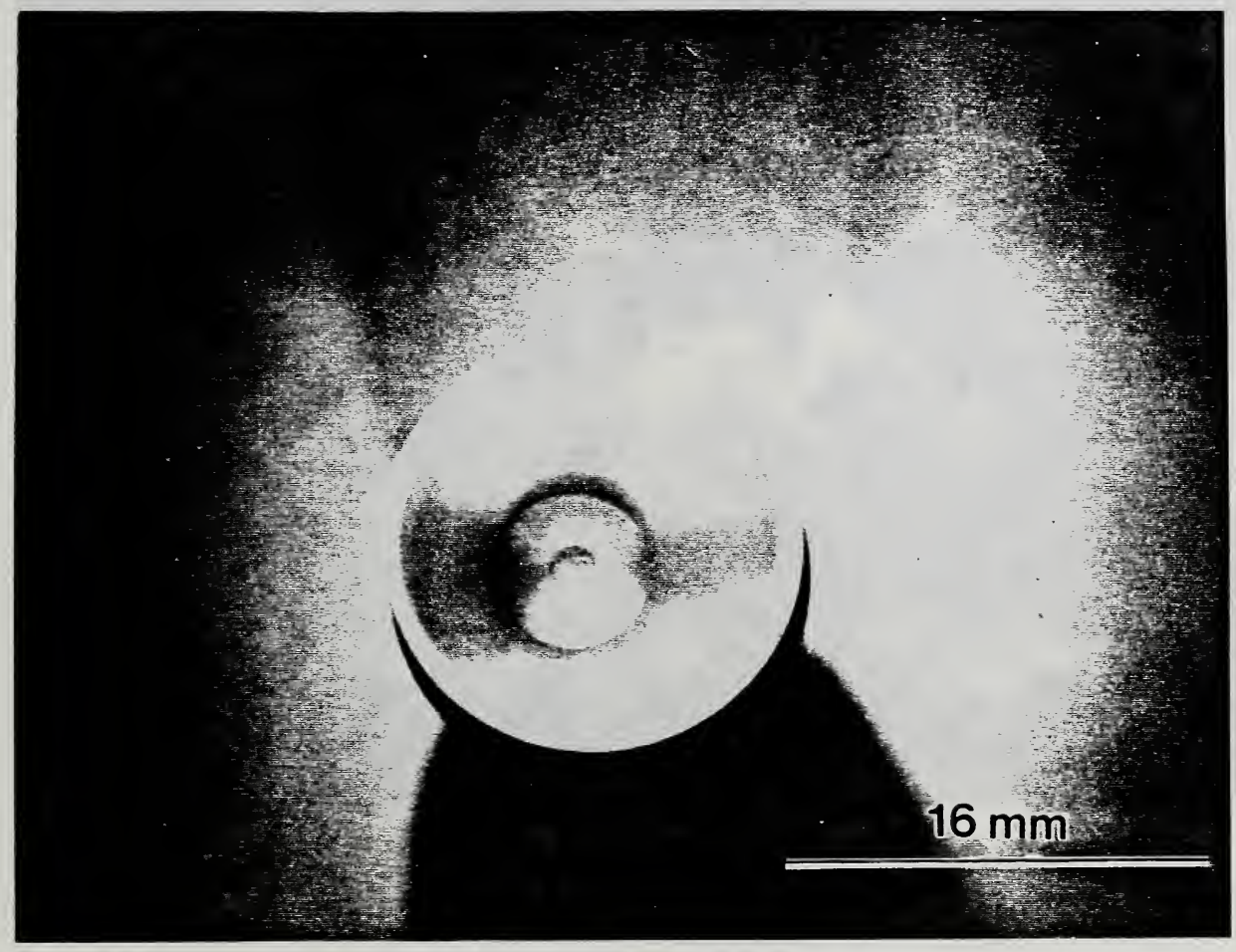

Figure 11. Melted aluminum ball of type used in reaction rate studies.

Figure 12. Surface of aluminum ball after reaction with ClO_3F at 800°C.

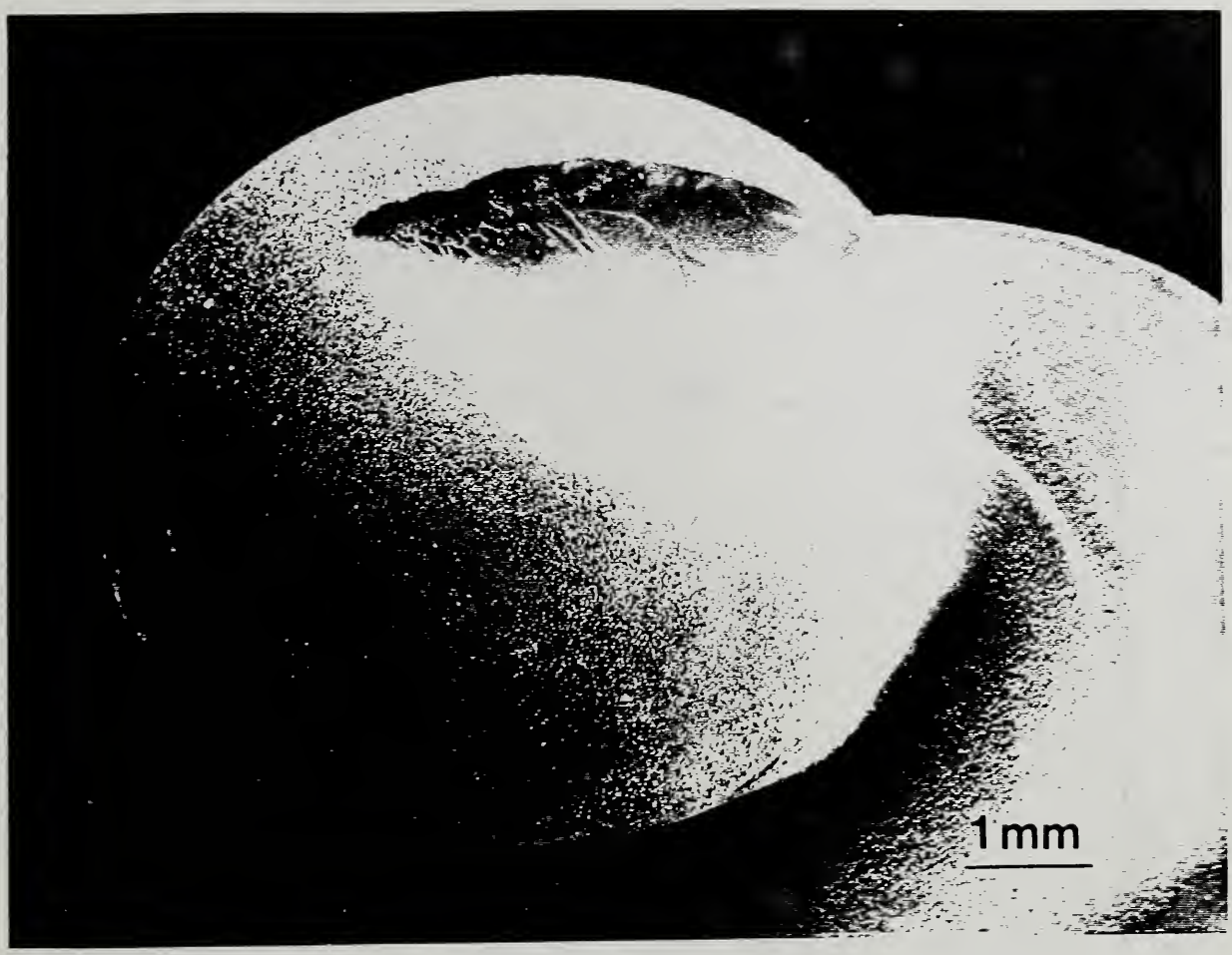

Figure 13. Surface of aluminum ball after ClO_3F reaction, showing surface channel under gas jet.

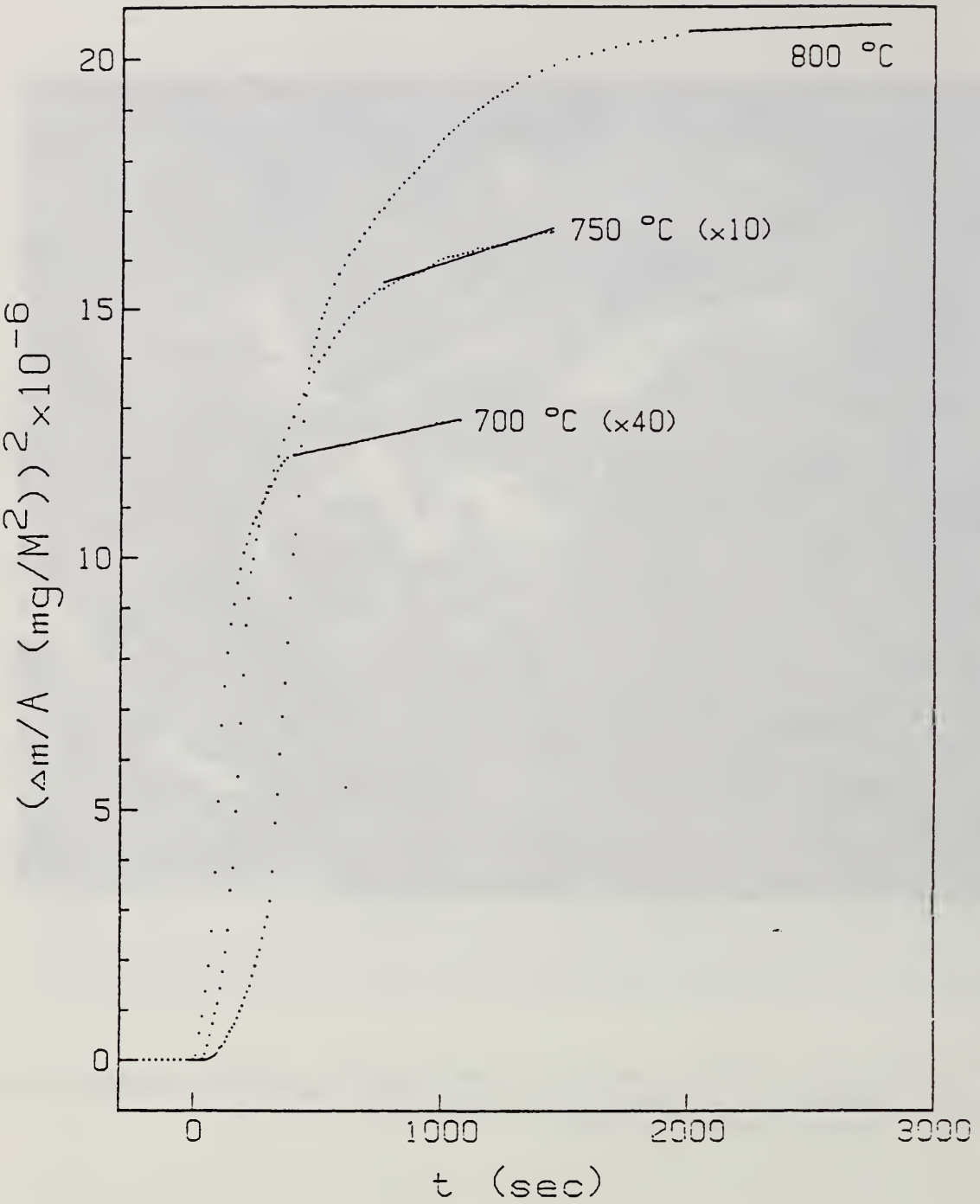

Figure 14. Thermogravimetric data for reaction of molten aluminum ball with ClO_3F at various temperatures.

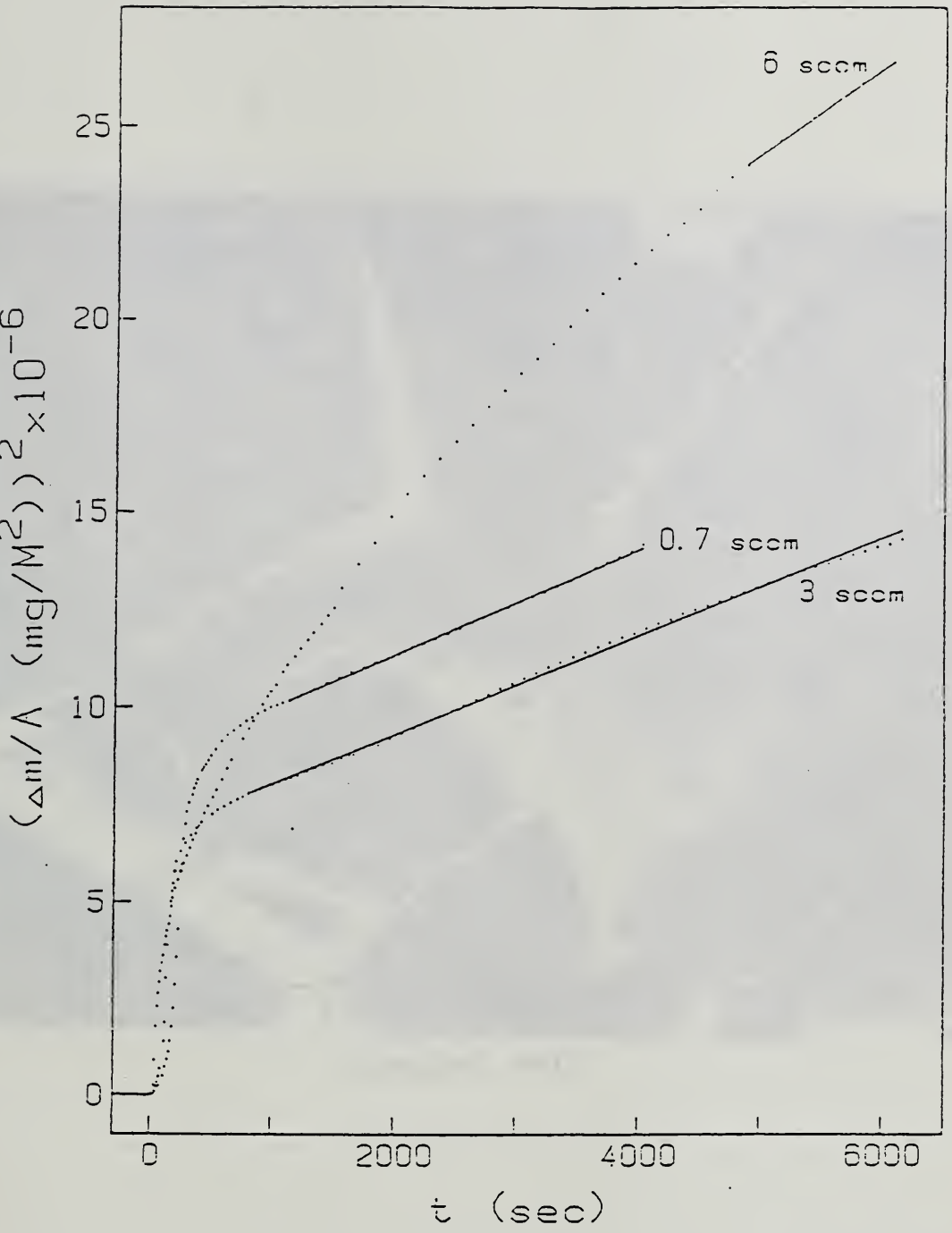

Figure 15. Thermogravimetric data for effect of ClO_3F flow rate on aluminum reaction at 800°C.

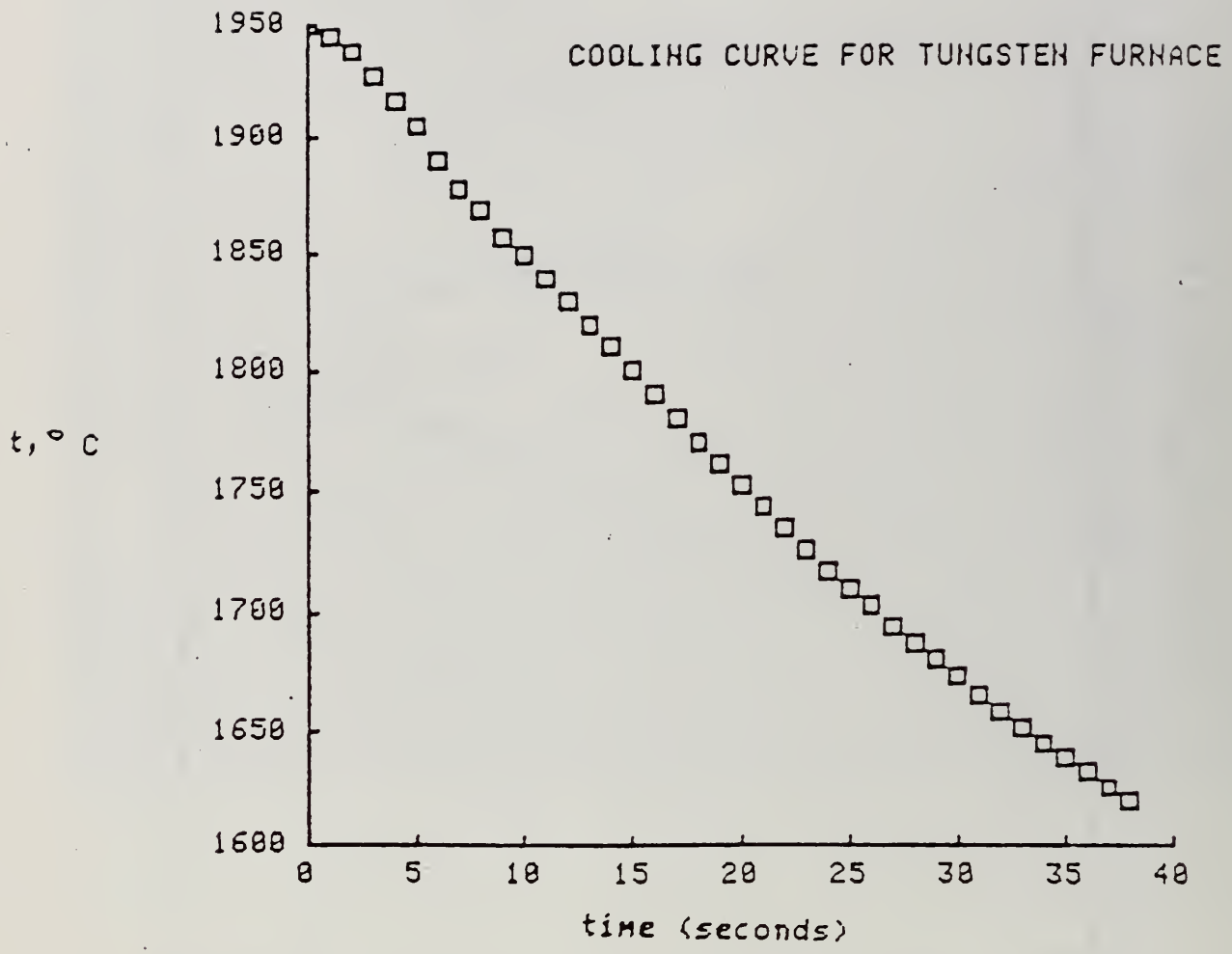

Figure 16. Cooling curve for tungsten furnace used in Li_2O-Al_2O_3 phase equilibrium experiments.

Figure 17. Equilibrium crystals of $LiAl_5O_8$ spinel with recrystallized interstitial eutectic melt.

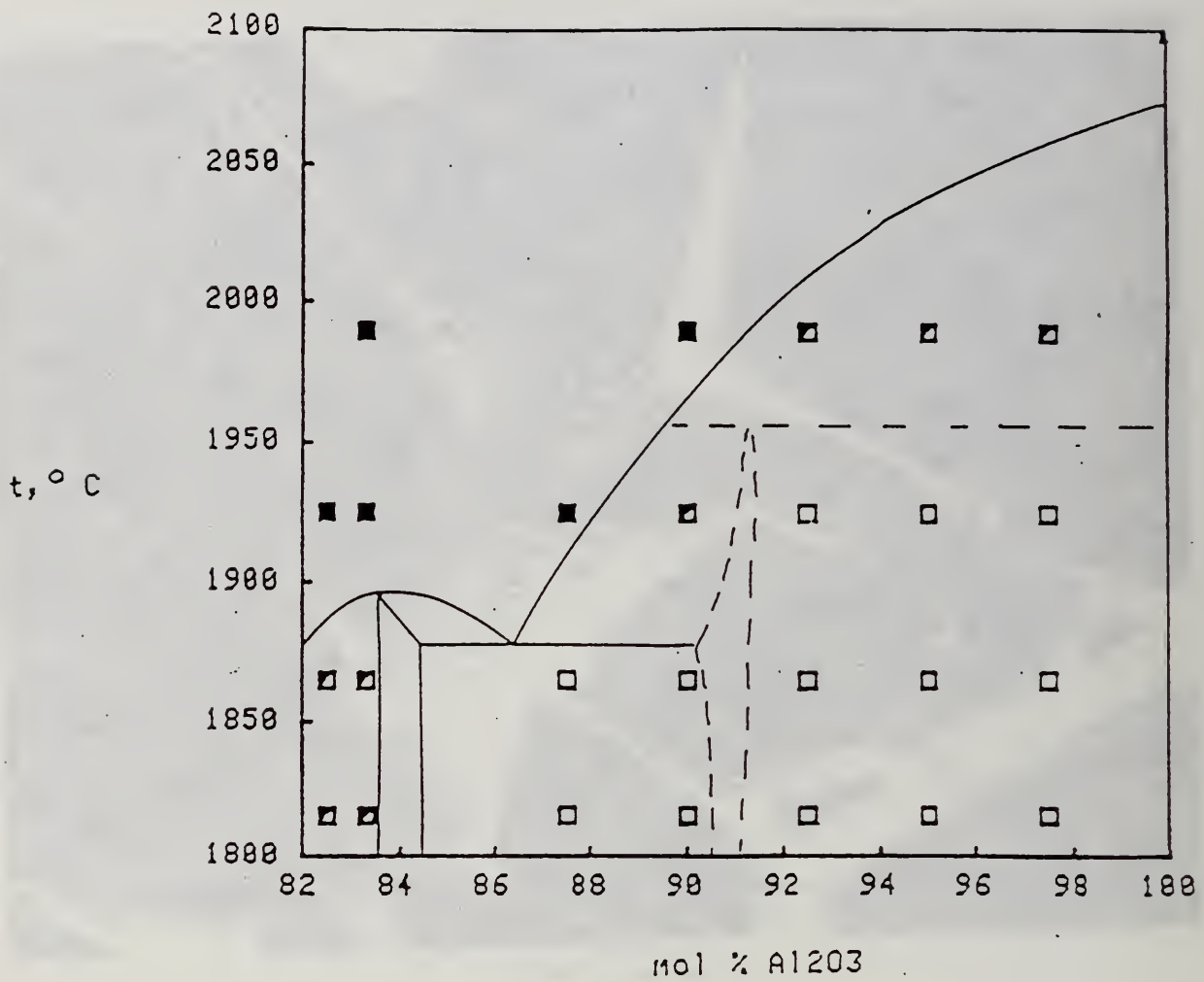

Figure 18. Phase diagram for the high alumina portion of the system $LiAlO_2$-Al_2O_3.

Figure 19. Lamellar intergrowths in $(Li_2O)_{2.5}$ $(Al_2O_3)_{97.5}$ cooled from 1925°C.

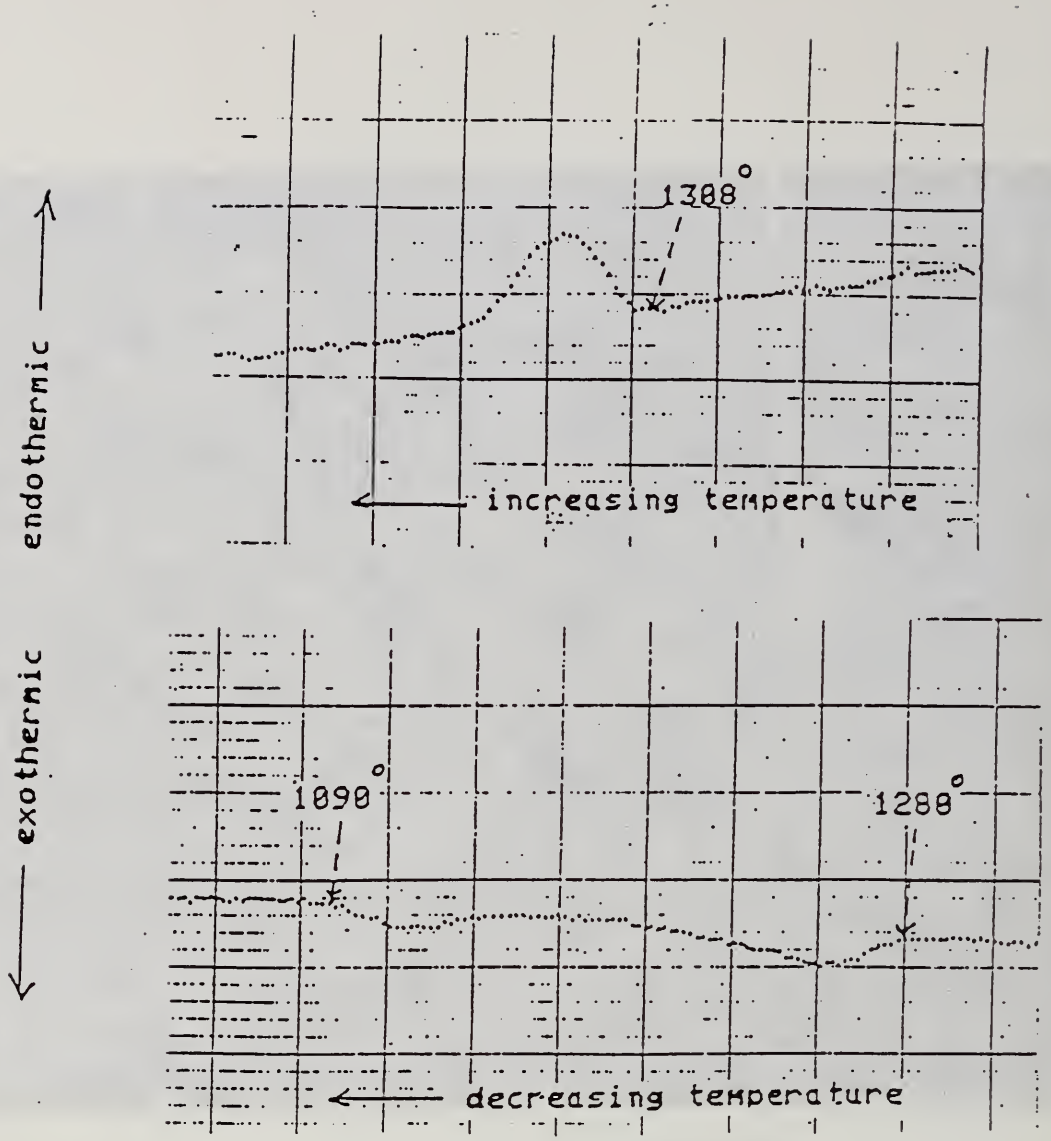

Figure 20. DTA analysis of phase transition in $LiAl_5O_8$.

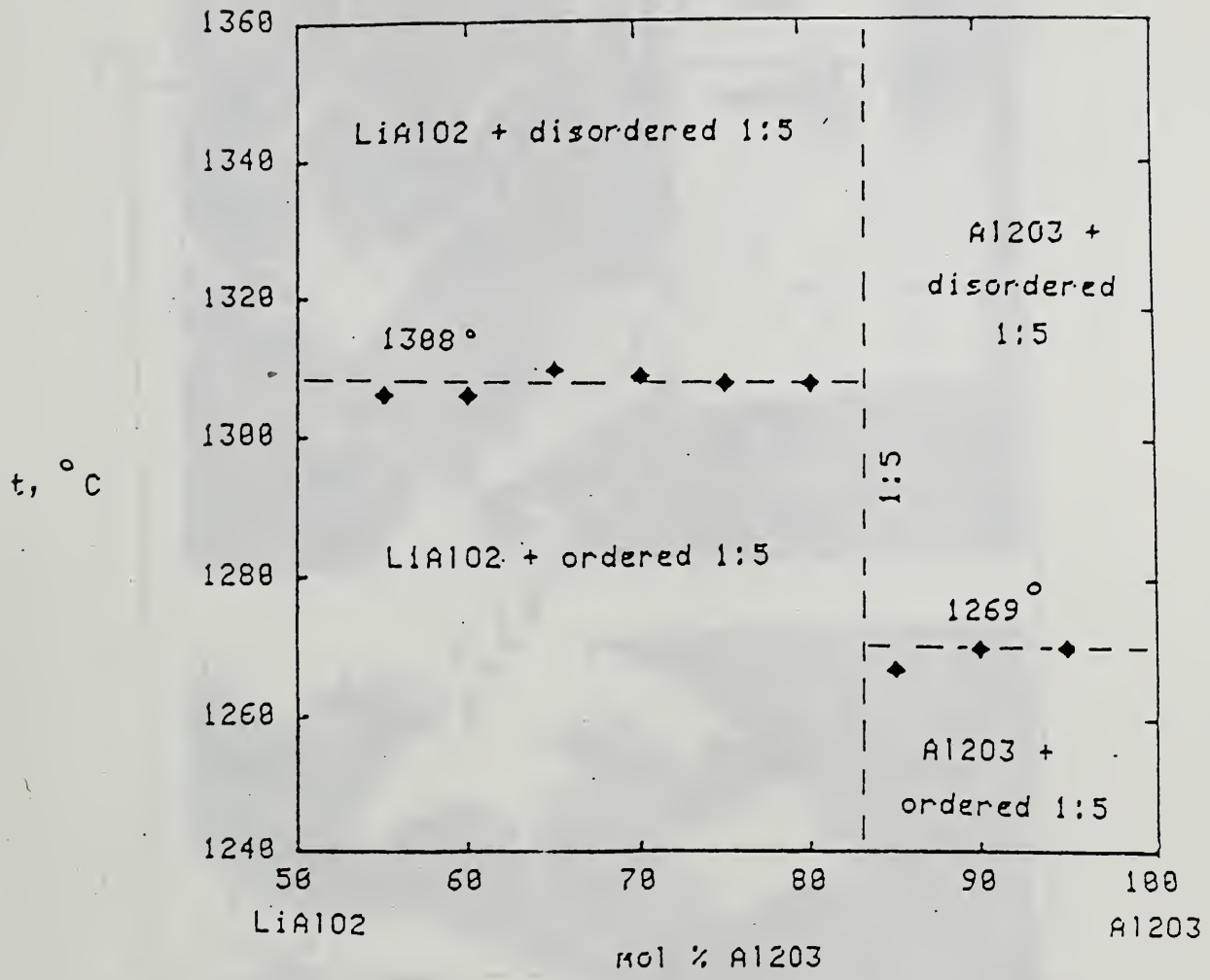

Figure 21. Effect of composition on $LiAl_5O_8$ transition.

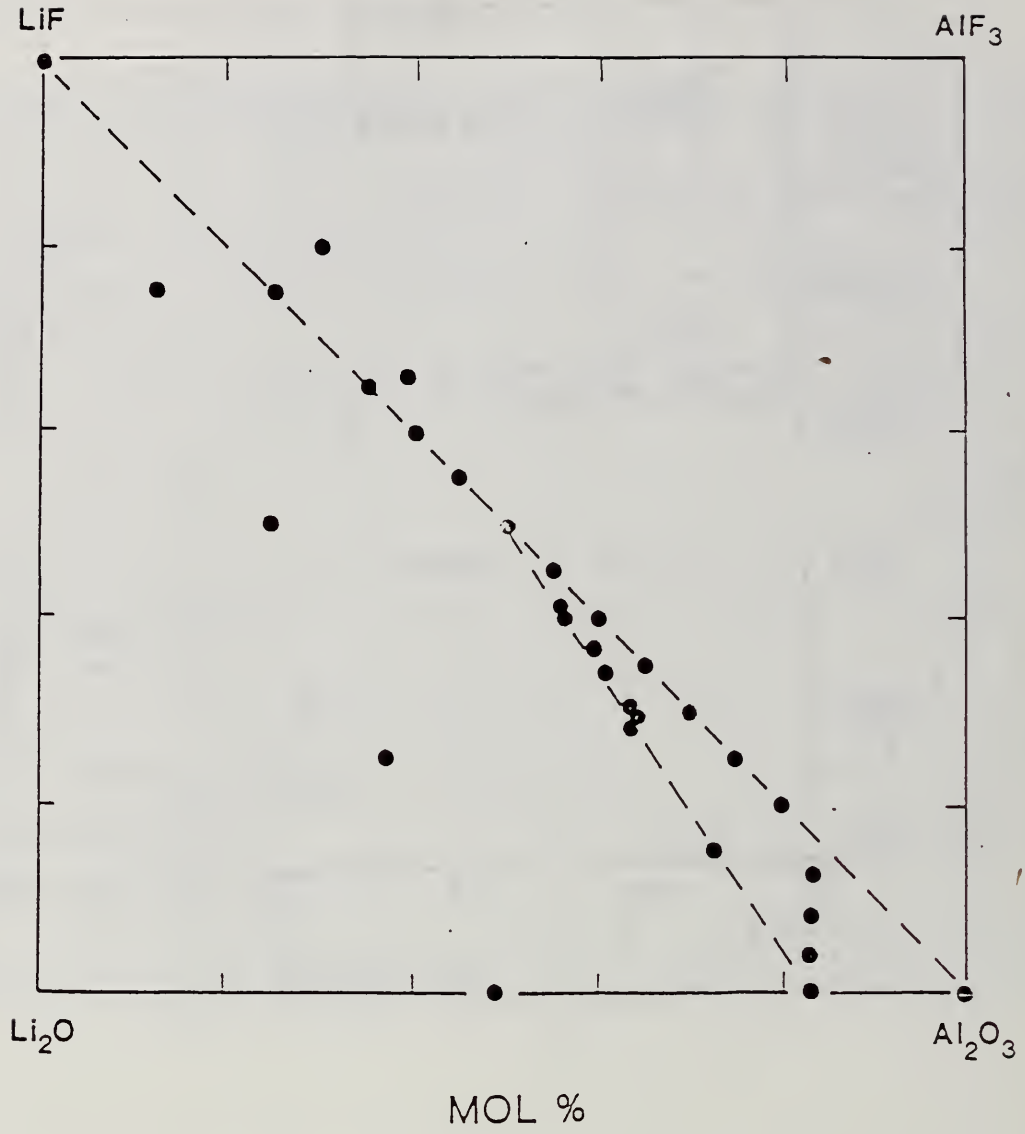

Figure 22. Compositions investigated in the system Li_2O-Al_2O_3-AlF_3-LiF.

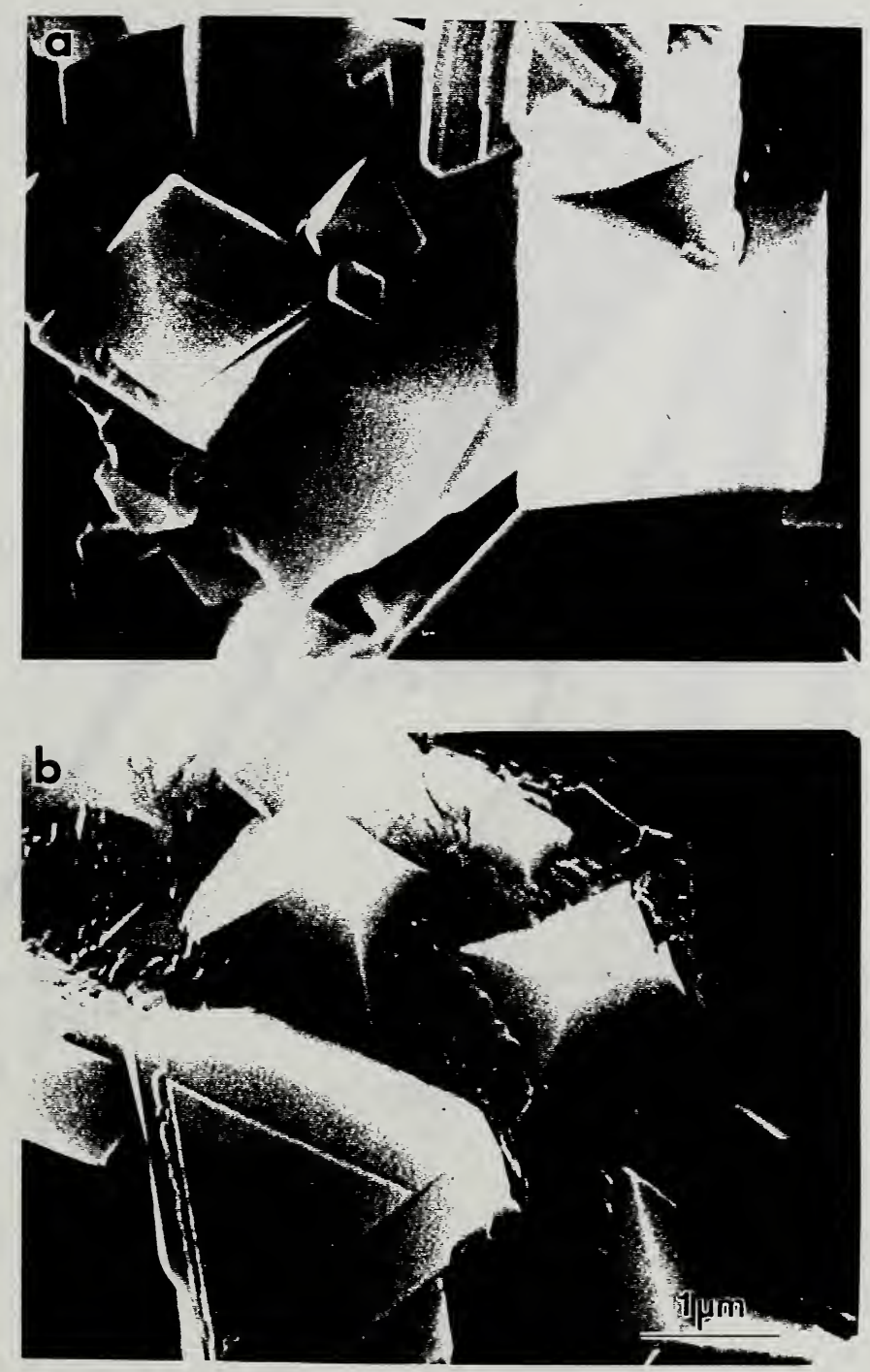

Figure 23. Effect of composition on melting at 1200°C in the system Li_2O-Al_2O_3-AlF_3-LiF. (a) composition $Li_7Al_7F_6O_{26}$ showing absence of melt; (b) composition $(LiF)_{50}$ $(Al_2O_3)_{50}$ showing definite melting.

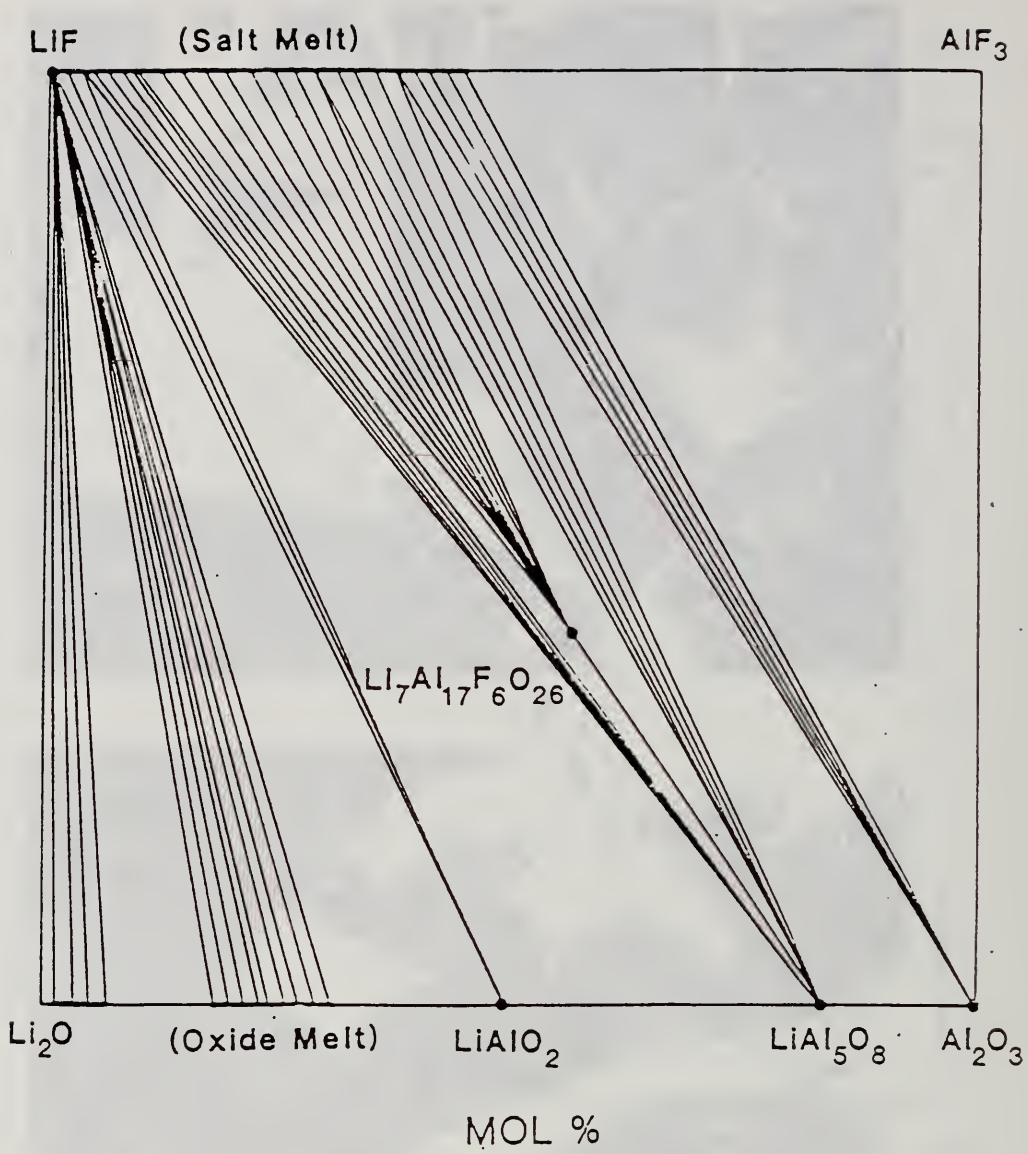

Figure 24. Phase relations in the system Li_2O-Al_2O_3-AlF_3-LiF at 1200°C.

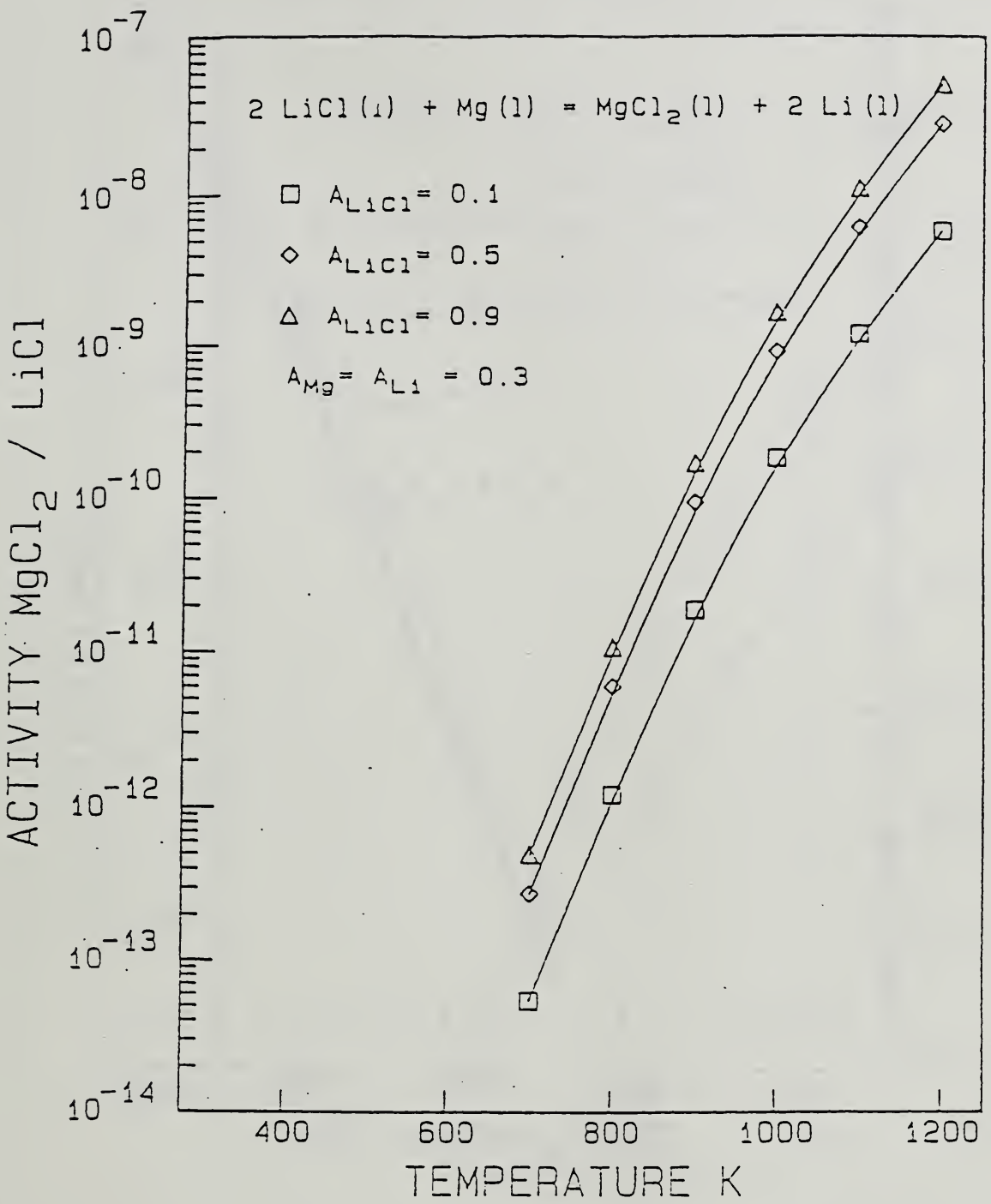

Figure 25. Calculated chemical equilibria of (Li, Mg) chlorides formed by reaction with LiMgAl alloy.

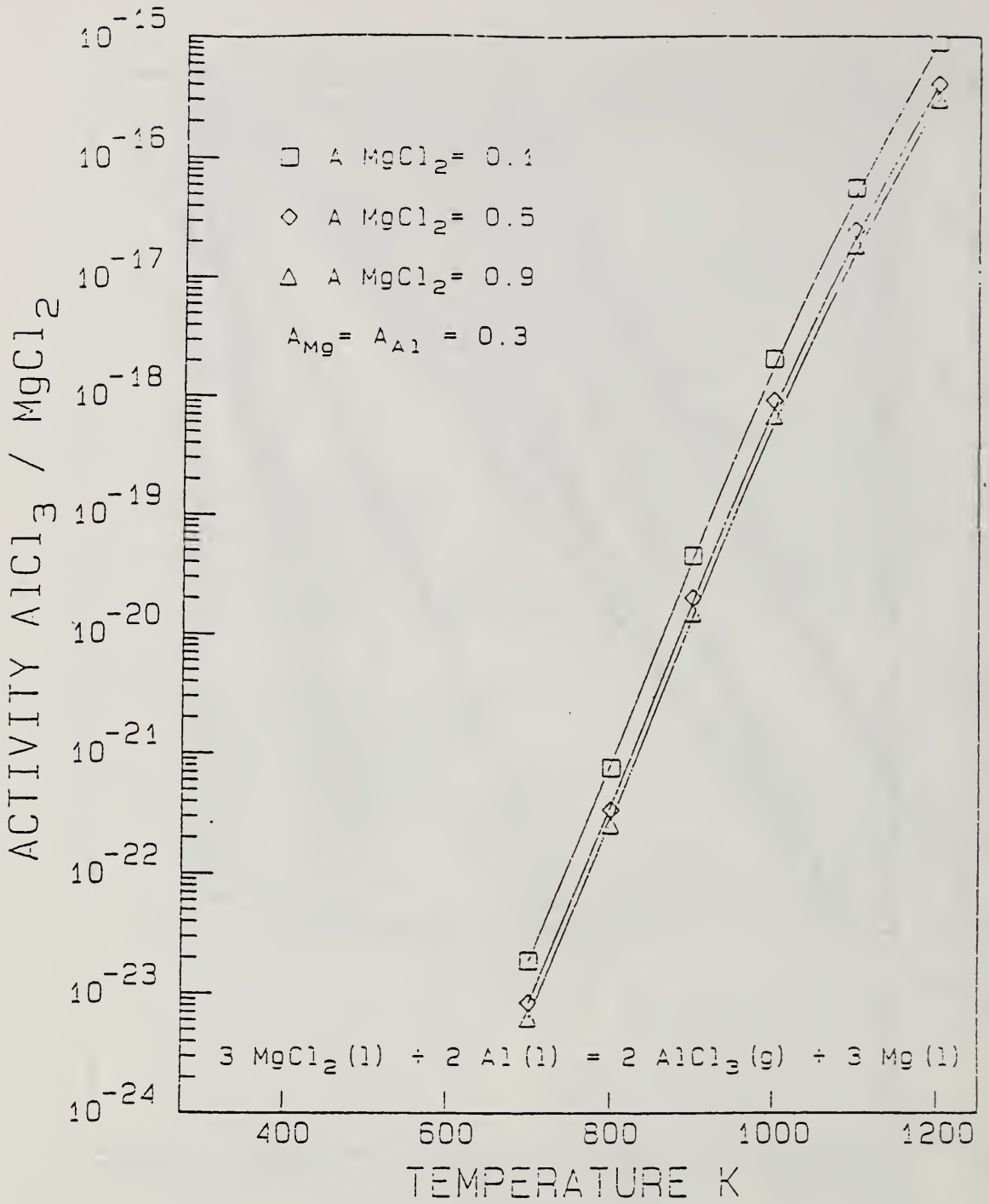

Figure 26. Calculated chemical equilibria of (Mg, Al) chlorides formed by reaction with LiMgAl alloy.

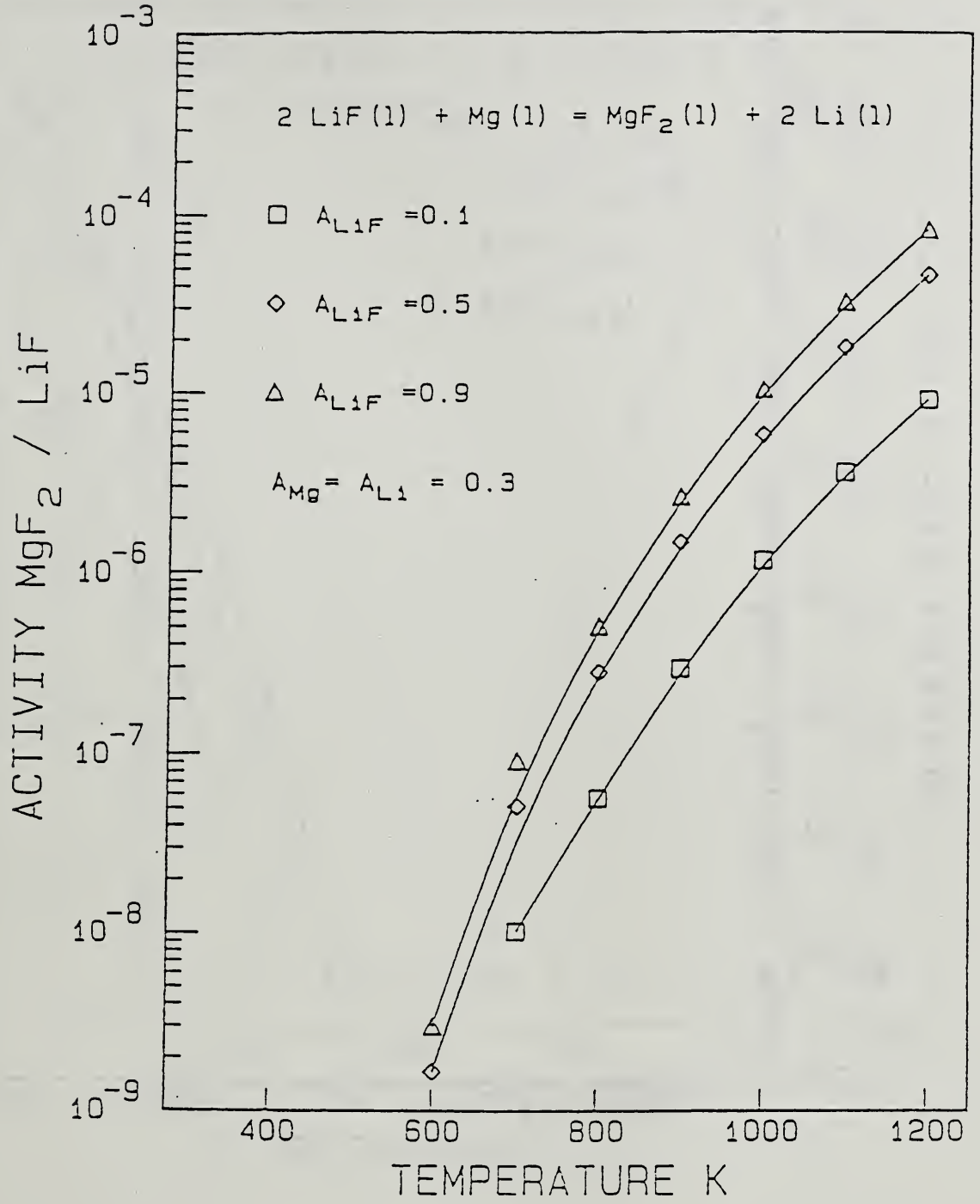

Figure 27. Calculated chemical equilibria of (Li, Mg) flourides formed by reaction with liMgAl alloy.

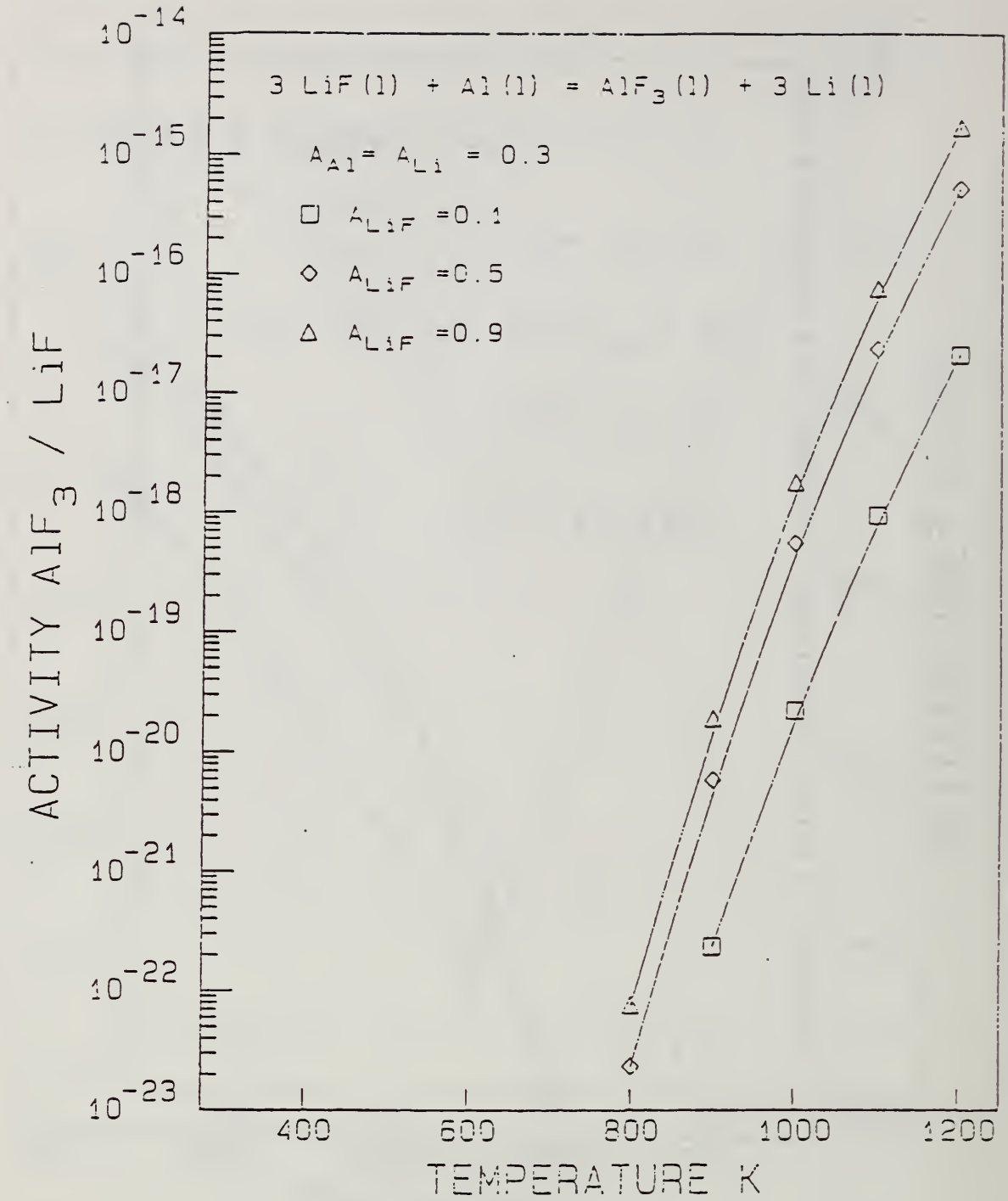

Figure 28. Calculated chemical equilibria of (Li, Al) flourides formed by reaction with LiMgAl alloy.

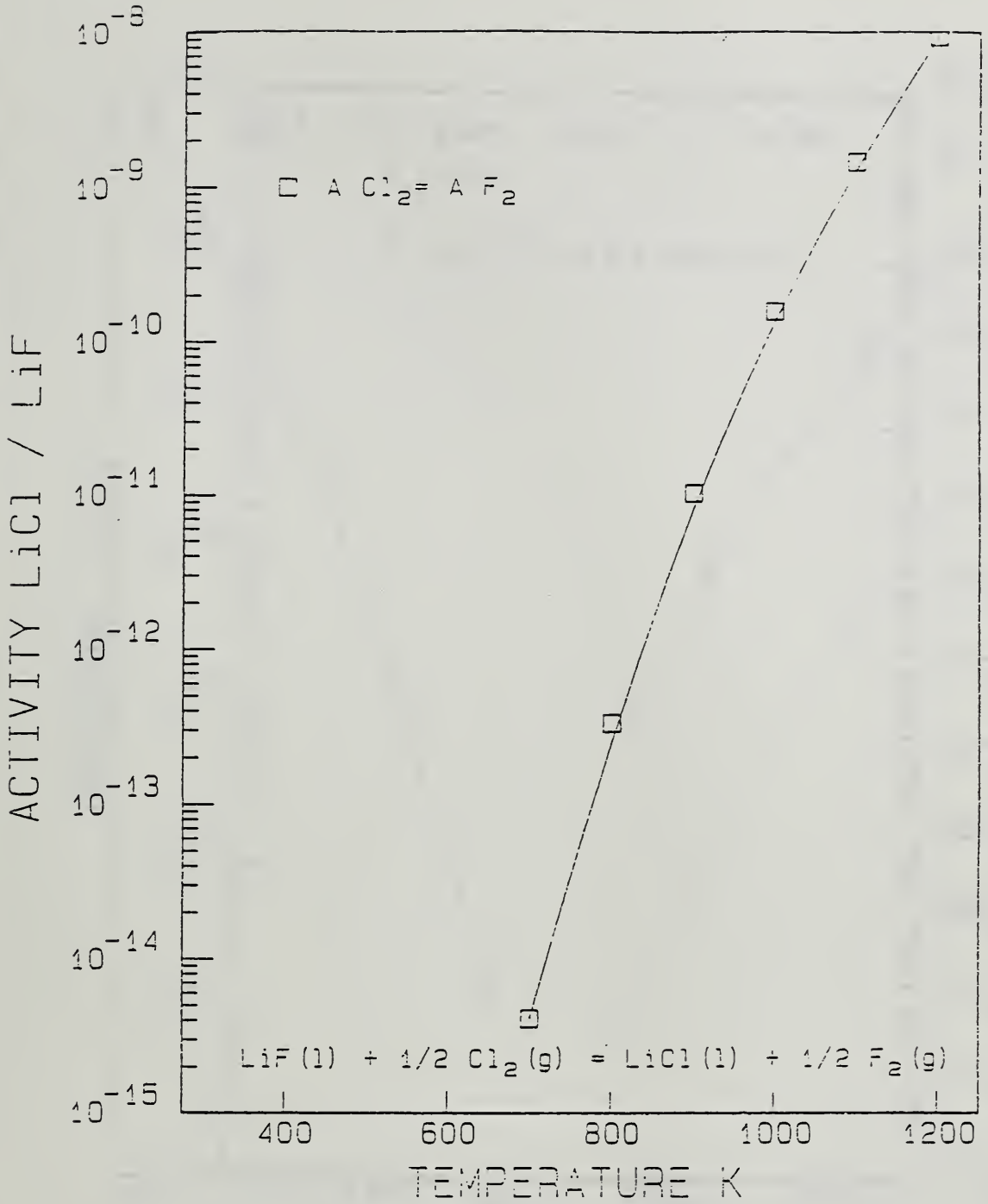

Figure 29. Calculated partitioning of flourine in the lithium molten salt phase.

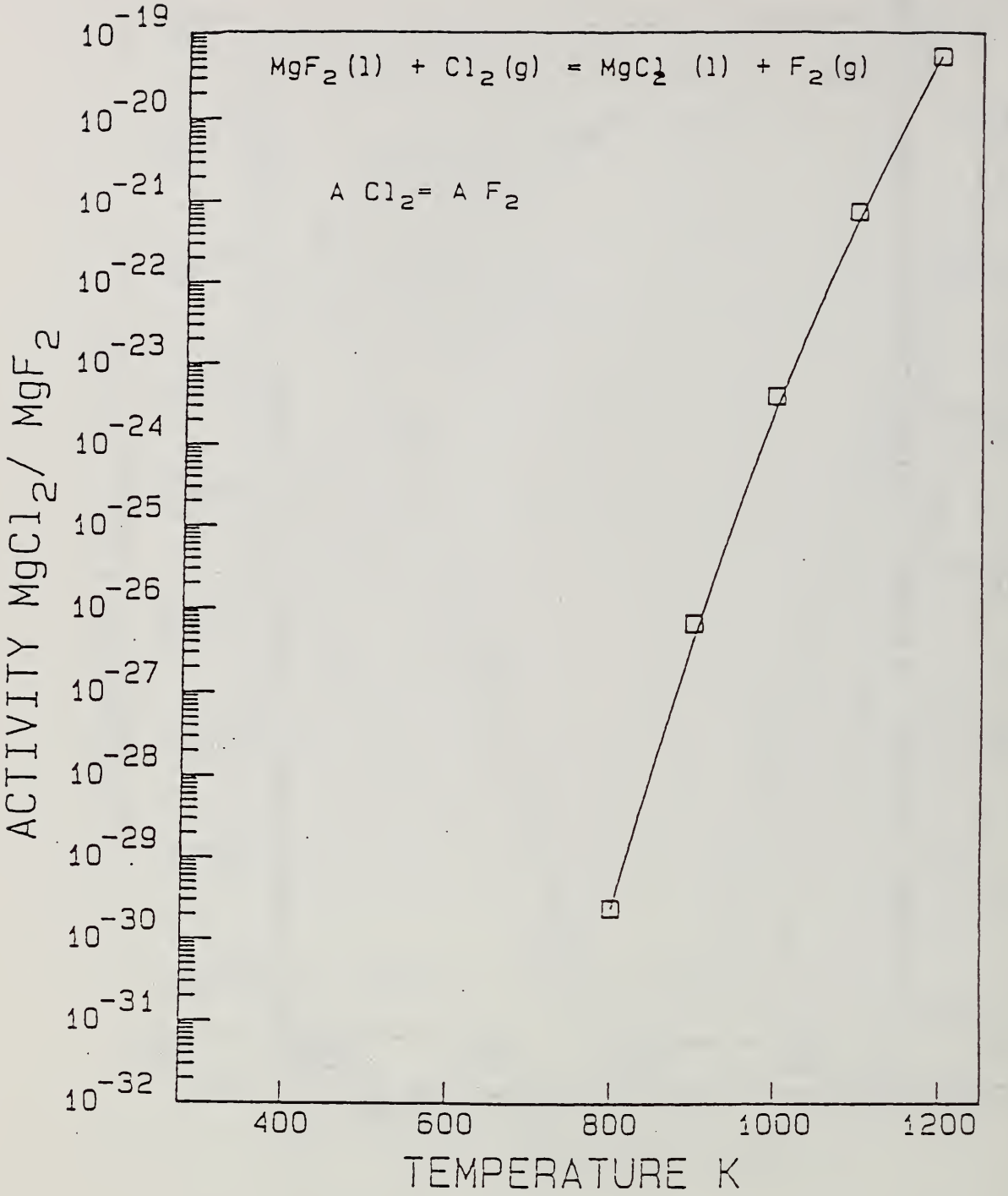

Figure 30. Calculated partitioning of flourine in the magnesium molten salt phase.

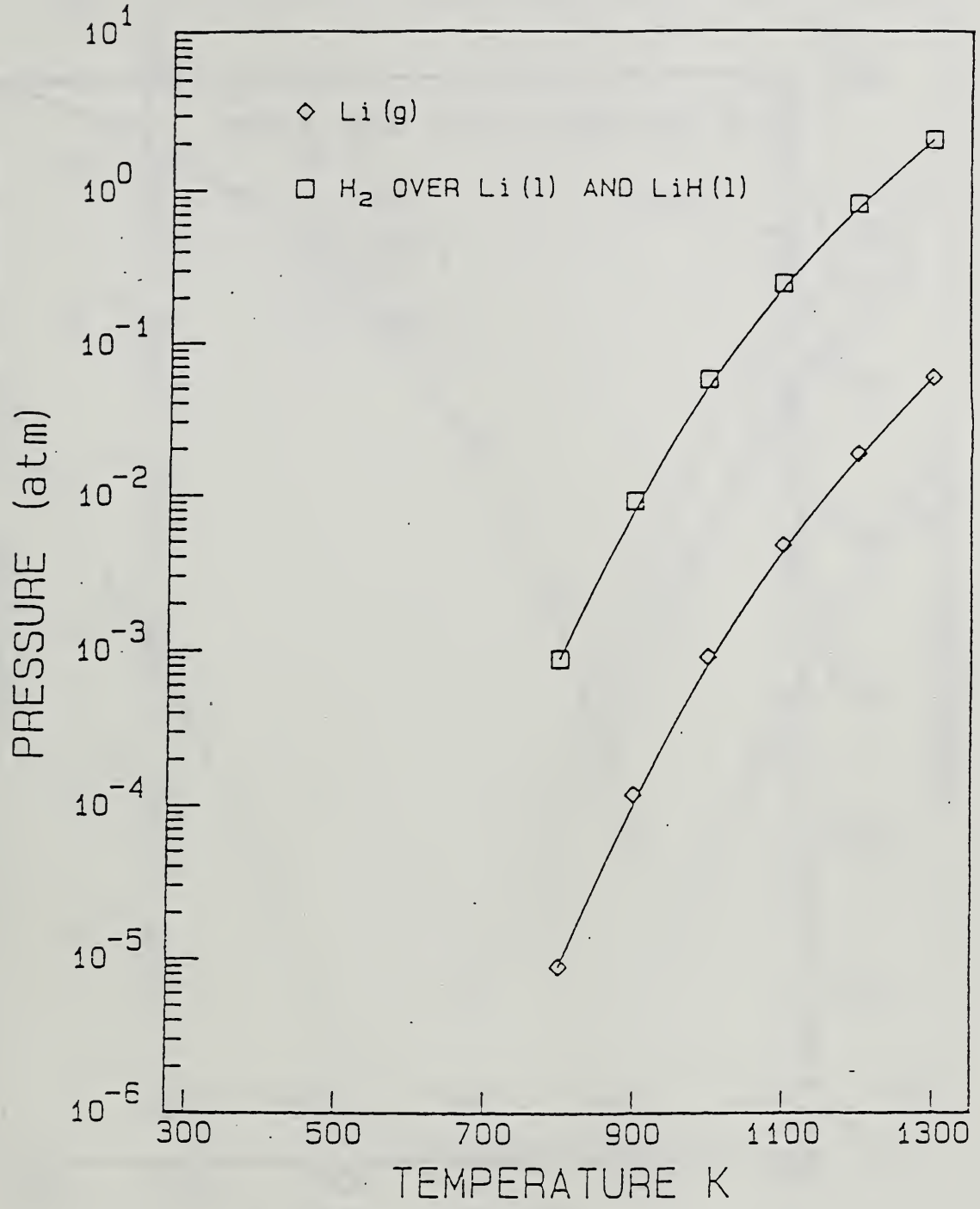

Figure 31. Calculated vapor pressures over molten lithium and over a Li + LiH mixture.

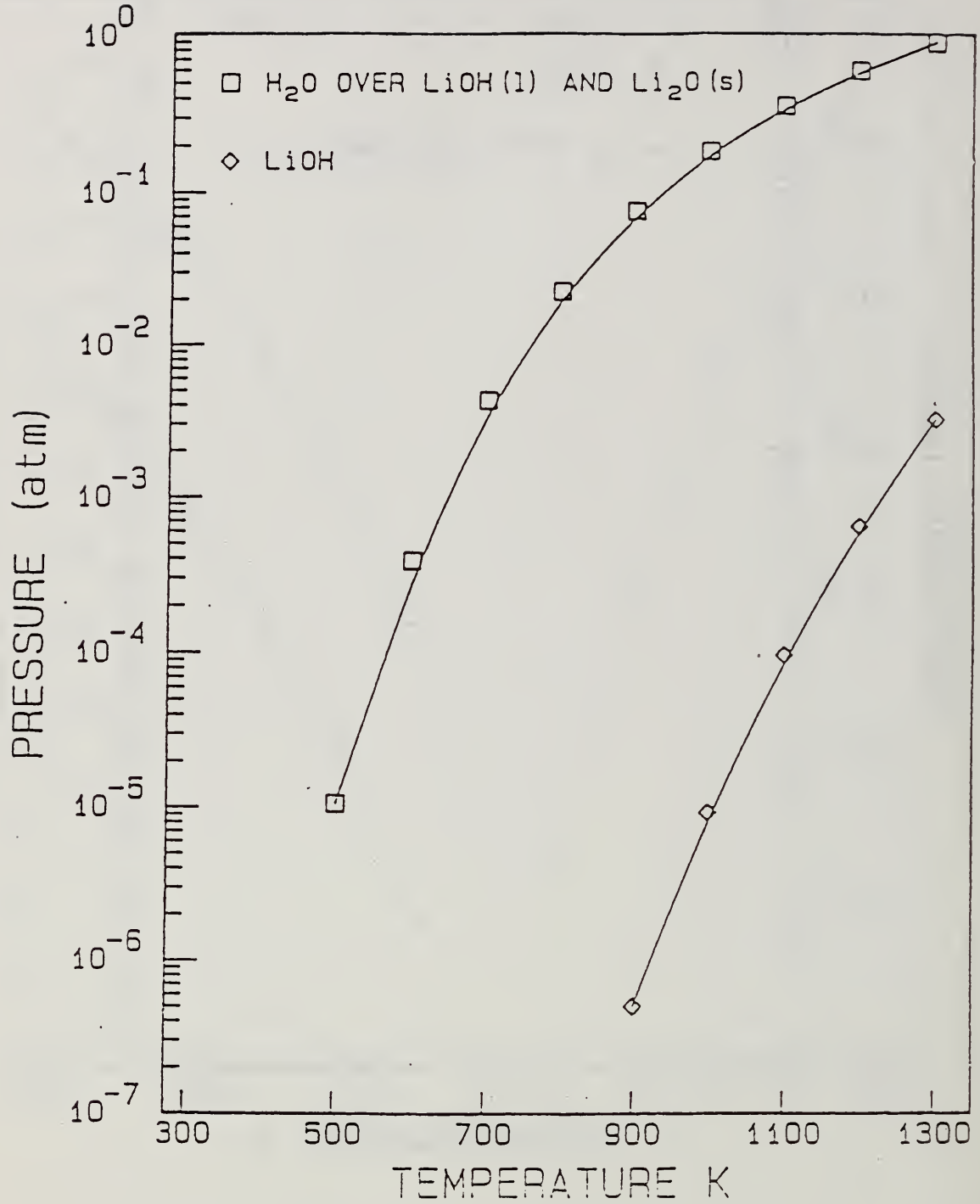

Figure 32. Calculated vapor pressures over LiOH and over a LiOH + Li_2O mixture.

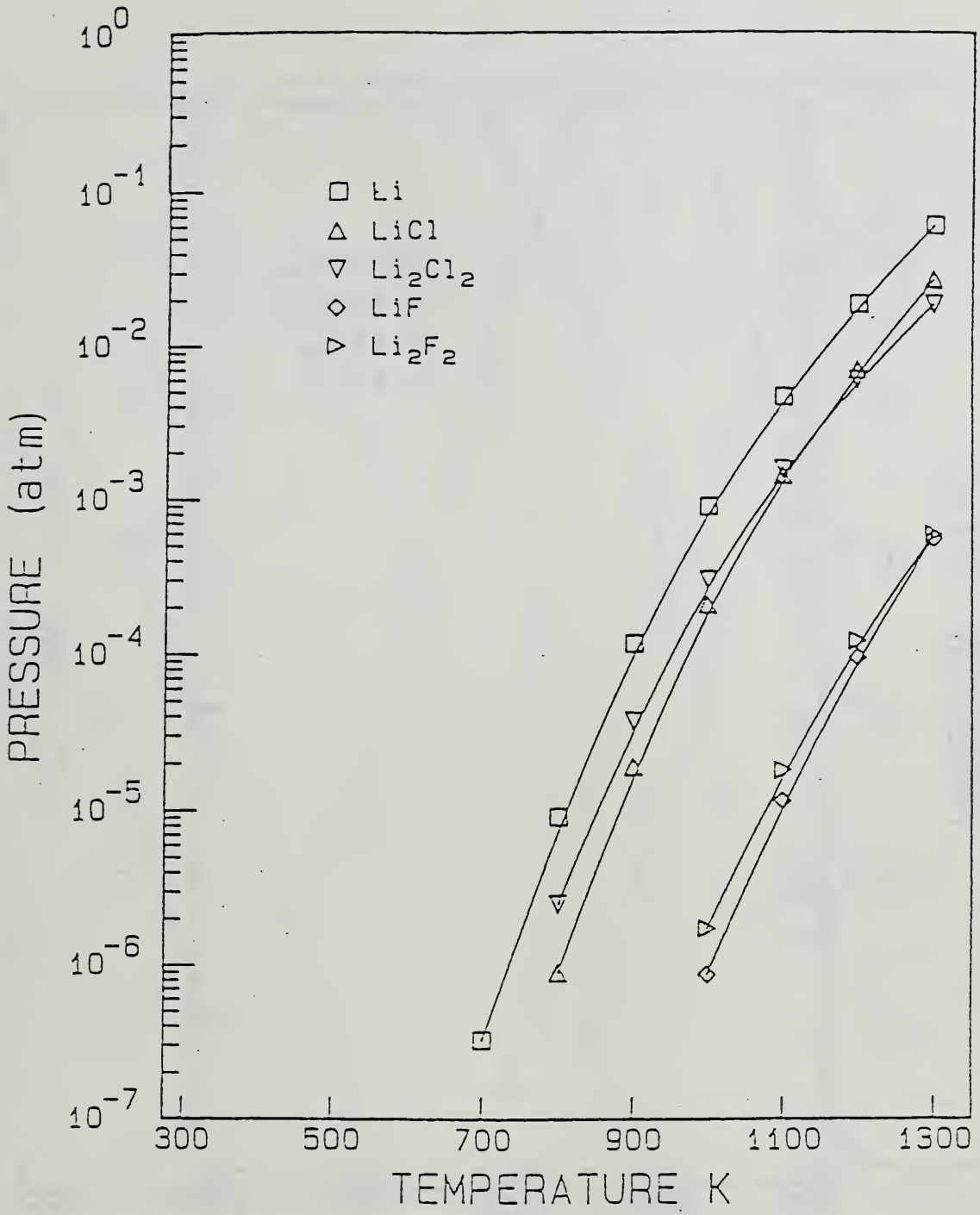

Figure 33. Calculated partial pressures of lithium species over their respective condensed phases.

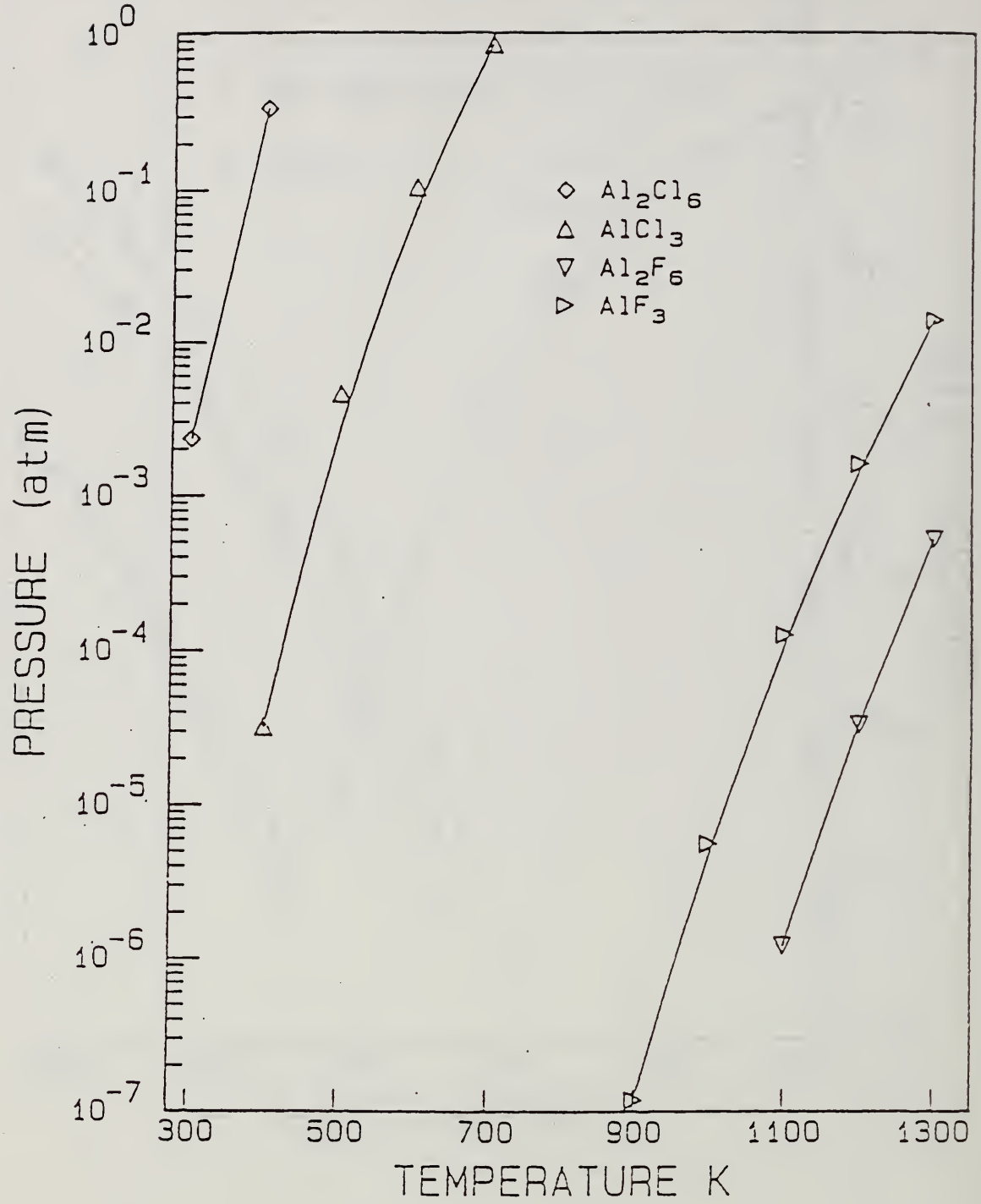

Figure 34. Calculated partial pressures of aluminum species over their respective condensed phases.

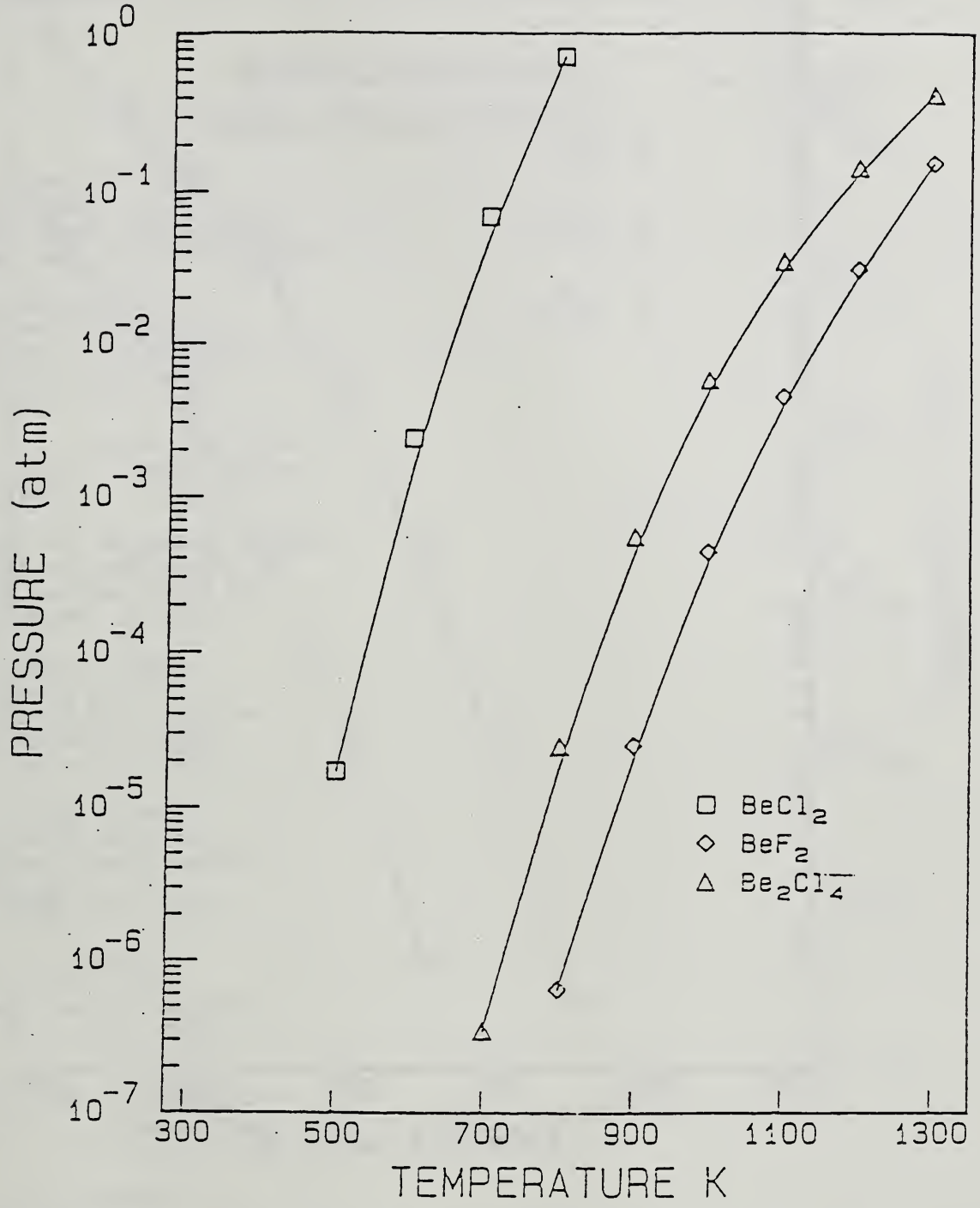

Figure 35. Calculated partial pressures of beryllium species over their respective condensed phases.

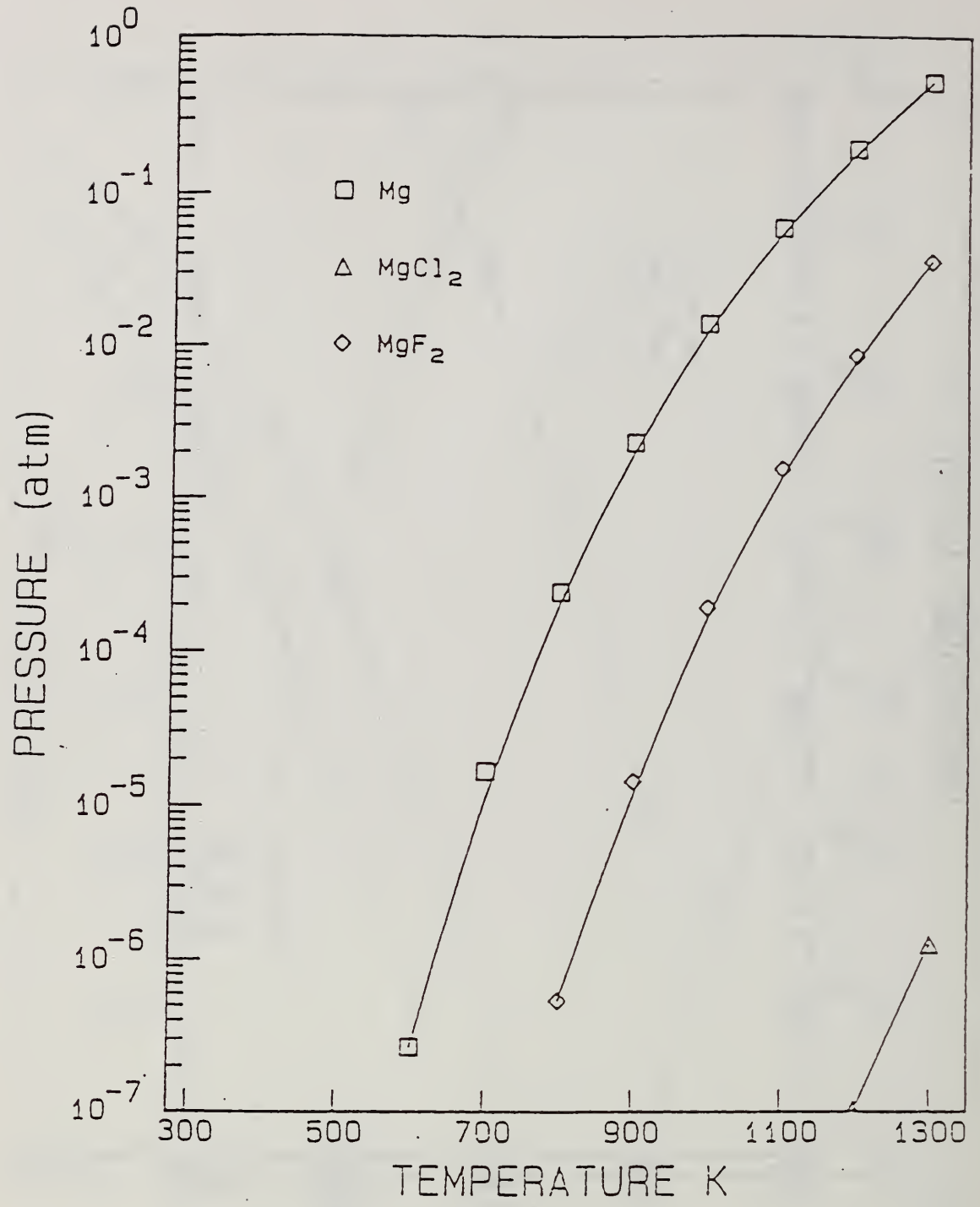

Figure 36. Calculated partial pressures of magnesium species over their respective condensed phases.

ONR REPORT DISTRIBUTION LIST

CLOSED, LIQUID METAL COMBUSTION

One copy except as noted

Dr. Lynn A. Parnell
Code 6341
Naval Ocean Systems Center
San Diego, California 92152
2

Dr. Richard Miller
Mechanics Division
Office of Naval Research
800 N. Quincy Street
Arlington, VA. 22217
2

Defense Documentation Center
Building 5, Cameron Station
Alexandria, VA. 22314
12

Technical Information Division
Naval Research Laboratory
4555 Overlook Avenue SW
Washington, DC 20375
6

Dr. Jerry A. Smith
Chemistry Division
Office of Naval Research
800 N. Quincy Street
Arlington, VA. 22217

Dr. Albert D. Wood
Technology Programs
Office of Naval Research
800 N. Quincy St.
Arlington, VA. 22217

Dr. H.W. Carhart
Combustion & Fuels
Naval Research Laboratory
Washington, DC 20375

Professor Allen Fuhs
Department of Aeronautics
Naval Post Graduate School
Monterey, California 93943

Division Director
Engineering and Weapons
US Naval Academy
Annapolis, Maryland 21402

Mr. Francis J. Romano
Code 63R3
Naval Sea Systems Command
Washington, DC 20363

One copy except
as noted

Mr. Norman D. Hubele
Fluidic Systems, MS 1301-RR
Garrett Pneumatic Systems Division
2801 East Washington St.
Phoenix, Arizona 85034

Dr. Hugh H. Darsie
Advanced Technology Group
Sunstrand Energy Systems
4747 Harrison Avenue
Rockford, Illinois 61101

Professor Gerard M. Faeth
Department of Aerospace Engineering
University of Michigan
Ann Arbor, Michigan 48109

Dr. Dan H. Kiely
Power & Energy Group
The Pennsylvania State University
Applied Research Laboratory
P.O. Box 30
State College, Pennsylvania 16801

Professor Darryl E. Metzger
Department of Mechanical &
Aerospace Engineering
Arizona State University
Tempe, Arizona 85281

Dr. Dae H. Cho
Reactor Analysis & Safety Division
Argonne National Laboratory
Argonne, Illinois 60439

Professor S.H. Chan
Department of Mechanical Engineering
The University of Wisconsin-Milwaukee
P.O. Box 784
Milwaukee, Wisconsin 53201

Professor George A. Brown
Department of Mechanical Engineering
and Applied Mechanics
University of Rhode Island
Kingston, Rhode Island 02881

One copy except
as noted

Professor A. Murty Kanury
Department of Mechanical Engineering
Oregon State University
Corvallis, Oregon 97331

Professor Irvin Glassman
Department of Mechanical & Aerospace Engineering
Engineering Quadrangle
Princeton University
Princeton, New York 08544

Professor Norman Chigier
Department of Mechanical Engineering
Carnegie-Mellon University
Pittsburgh, Pennsylvania 15213

Professor George Janz
Cogswell Laboratory, R306
Department of Chemistry
Rensselaer Polytechnic Institute
Troy, New York 12181

Dr. Leonard Leibowitz
Chemical Technology Division
Argonne National Laboratory
9700 South Case Avenue
Argonne, Illinois 60439

Professor John Tarbell
104 Fenske Laboratory
Pennsylvania State University
University Park, Pennsylvania 16801

Professor Thomas E. Daubert
104 Fenske Laboratory
Pennsylvania State University
University State Park, Pennsylvania 16801

Dr. J. Braunstein
Research Division
Oak Ridge Operations
Department E
Oak Ridge, Tennessee 37831

One copy except
as noted

Mr. Robert Tompkins
Code 36621, Bldg 126T
Naval Underwater Systems Center
Newport, Rhode Island 02841

Mr. Maurice F. Murphy
Code R33, Room 4-1711
Naval Surface Weapons, White Oak
Silver Spring, Maryland 20910

Dr. Kurt Mueller
Code R10
Energetic Materials Division
Naval Surface Weapons Center, White Oak
Silver Spring, Maryland 20910

Dr. Earl Quandt, Jr.
Code 2704
David Taylor Naval Ship
Research and Development Center
Annapolis, MD 21402

Mr. Richard Bloomquist
Code 2752
David Taylor Naval Ship R&D Center
Annapolis, Maryland 21402

Dr. Lawrence P. Cook
High Temperature Processes Group
National Bureau of Standards
Washington, DC 20234

Dr. W. Lee
Research and Technology Department
Naval Surface Weapons Center
Silver Spring, MD 20703

NBS-114A (REV. 2-8C)

U.S. DEPT. OF COMM. BIBLIOGRAPHIC DATA SHEET (See instructions)	1. PUBLICATION OR REPORT NO. NBSIR 87-3601	2. Performing Organ. Report No.	3. Publication Date JULY 1987

4. TITLE AND SUBTITLE

High Temperature Chemistry of Stored Chemical Energy Reactions for Propulsion

5. AUTHOR(S)

L. P. Cook, E. R. Plante, D. W. Bonnell, J. W. Hastie

6. PERFORMING ORGANIZATION (If joint or other than NBS, see instructions)

NATIONAL BUREAU OF STANDARDS
U.S. DEPARTMENT OF COMMERCE
GAITHERSBURG, MD 20899

7. Contract/Grant No.

8. Type of Report & Period Covered

9. SPONSORING ORGANIZATION NAME AND COMPLETE ADDRESS (Street, City, State, ZIP)

Office of Naval Research
800 N. Quincy Street
Arlington, VA 22217

10. SUPPLEMENTARY NOTES

☐ Document describes a computer program; SF-185, FIPS Software Summary, is attached.

11. ABSTRACT (A 200-word or less factual summary of most significant information. If document includes a significant bibliography or literature survey, mention it here)

This report summarizes the results of a continuing study of the high temperature chemistry of stored chemical energy reaction systems. The eight fuel/oxidant reactions of interest (including several which are multistage) are: Li/H_2O, H_2/O_2, NaO_2/H_2O, LiB/NF_3. Thermodynamic prediction of the products of three of these reactions has been corroborated by equilibrating postulated products at high temperature, while results from a fourth reaction require modification of the reaction scheme originally proposed. Mass spectrometric observations on the thermal decomposition of ClO_3F at elevated temperatures are presented. Thermogravimetric studies have been completed on the behavior of Al_2O_3 and MgO in the presence of ClO_3F and on the oxidation of molten aluminum droplets by ClO_3F. The solid state phase transition in $LiAl_2O_8$ has been studied by DTA. In the ClO_3F-based reaction systems, substantial entry of fluorine into the product $LiAl_5O_8$ spinel phase is postulated.

Thermodynamic calculations have been completed to assess the importance of vaporization of reactant/product solids and liquids.

12. KEY WORDS (Six to twelve entries; alphabetical order; capitalize only proper names; and separate key words by semicolons)

Al_2O_3; aluminum; kinetics; Li_2O; lithium; magnesium; mass spectrometry; perchloryl fluoride; phase equilibria; stored chemical energy reactions; thermal analysis;

13. AVAILABILITY

☒ Unlimited

☐ For Official Distribution. Do Not Release to NTIS

☐ Order From Superintendent of Documents, U.S. Government Printing Office, Washington, D.C. 20402.

☒ Order From National Technical Information Service (NTIS), Springfield, VA. 22161

14. NO. OF PRINTED PAGES

94

15. Price

$13.95

USCOMM-DC 6043-P80